ETSI GR ISC 002 V1.1.1 (2025-08)

GROUP REPORT

Integrated Sensing And Communications (ISAC); Channel Modelling, Measurements and Evaluation Methodology

Disclaimer

The present document has been produced and approved by the Integrated Sensing And Communications (ISAC) ETSI Industry Specification Group (ISG) and represents the views of those members who participated in this ISG.
It does not necessarily represent the views of the entire ETSI membership.

Reference
DGR/ISC-002

Keywords
channel modelling, evaluation, ISAC,
measurement

ETSI

650 Route des Lucioles
F-06921 Sophia Antipolis Cedex - FRANCE

Tel.: +33 4 92 94 42 00 Fax: +33 4 93 65 47 16

Siret N° 348 623 562 00017 - APE 7112B
Association à but non lucratif enregistrée à la
Sous-Préfecture de Grasse (06) N° w061004871

Contents

Intellectual Property Rights

Essential patents

IPRs essential or potentially essential to normative deliverables may have been declared to ETSI. The declarations pertaining to these essential IPRs, if any, are publicly available for **ETSI members and non-members**, and can be found in ETSI SR 000 314: *"Intellectual Property Rights (IPRs); Essential, or potentially Essential, IPRs notified to ETSI in respect of ETSI standards"*, which is available from the ETSI Secretariat. Latest updates are available on the ETSI IPR online database.

Pursuant to the ETSI Directives including the ETSI IPR Policy, no investigation regarding the essentiality of IPRs, including IPR searches, has been carried out by ETSI. No guarantee can be given as to the existence of other IPRs not referenced in ETSI SR 000 314 (or the updates on the ETSI Web server) which are, or may be, or may become, essential to the present document.

Trademarks

The present document may include trademarks and/or tradenames which are asserted and/or registered by their owners. ETSI claims no ownership of these except for any which are indicated as being the property of ETSI, and conveys no right to use or reproduce any trademark and/or tradename. Mention of those trademarks in the present document does not constitute an endorsement by ETSI of products, services or organizations associated with those trademarks.

DECT™, **PLUGTESTS™**, **UMTS™** and the ETSI logo are trademarks of ETSI registered for the benefit of its Members. **3GPP™**, **LTE™** and **5G™** logo are trademarks of ETSI registered for the benefit of its Members and of the 3GPP Organizational Partners. **oneM2M™** logo is a trademark of ETSI registered for the benefit of its Members and of the oneM2M Partners. **GSM**® and the GSM logo are trademarks registered and owned by the GSM Association.

Foreword

This Group Report (GR) has been produced by ETSI Industry Specification Group (ISG) Integrated Sensing And Communications (ISAC).

Modal verbs terminology

In the present document "**should**", "**should not**", "**may**", "**need not**", "**will**", "**will not**", "**can**" and "**cannot**" are to be interpreted as described in clause 3.2 of the ETSI Drafting Rules (Verbal forms for the expression of provisions).

"**must**" and "**must not**" are **NOT** allowed in ETSI deliverables except when used in direct citation.

Executive summary

The present document provides an overview of the current state-of-the-art in ISAC channel modelling approaches and summarizes their key limitations.

In addition, the present document provides ISAC channel modelling enhancements, including RCS modelling for complex objects, micro-Doppler modelling for small-scale motion recognition, micro-deformation modelling for structural health monitoring, and rainfall attenuation modelling for power loss caused by precipitation.

Finally, the present document presents conclusions and recommendations for future work addressing required developments for ISAC systems and radio access network architectures, including security, privacy, trustworthiness, and sustainability.

Introduction

There is growing interest in ISAC across the broader research ecosystem, including global standardization bodies, industrial stakeholders, academia, and regional collaborative projects. The present document provides a study on ISAC channel modelling, which can serve as a basis for evaluating the performance of future 6G ISAC solutions.

1 Scope

The present document outlines the scope as follows:

- Develop advanced ISAC channel models and validation through measurement campaigns and emulations, that can fill the gaps of existing channel models.
- Validate the models through feasibility analysis and measurement campaign.
- Identify and describe the corresponding use cases and the potentially suitable frequency bands.

2 References

2.1 Normative references

Normative references are not applicable in the present document.

2.2 Informative references

References are either specific (identified by date of publication and/or edition number or version number) or non-specific. For specific references, only the cited version applies. For non-specific references, the latest version of the referenced document (including any amendments) applies.

NOTE: While any hyperlinks included in this clause were valid at the time of publication, ETSI cannot guarantee their long-term validity.

The following referenced documents may be useful in implementing an ETSI deliverable or add to the reader's understanding, but are not required for conformance to the present document.

[i.1] IEEE 802.11-21bf™: "Channel Models for WLAN Sensing Systems".

[i.2] ETSI TR 138 901 (V18.0.0): "5G; Study on channel model for frequencies from 0.5 to 100 GHz (3GPP TR 38.901 version 18.0.0 Release 18)".

[i.3] Chen Victor C. et al.: "Micro-Doppler effect in radar: phenomenon, model, and simulation study", IEEE™ Transactions on Aerospace and electronic systems, vol. 42.1, pp. 2-21, 2006.

[i.4] Liu Ting et al.: "Channel Modelling on Micro-Doppler Feature of a Pedestrian at 77 GHz", IEEE™ Conference on Antenna Measurements and Applications (CAMA). IEEE™, 2023.

[i.5] Tahmoush Dave: "Review of micro-Doppler signatures", IEEE™ Conference on Antenna Measurements and Applications (CAMA), 2023.

[i.6] Chen Victor C.: "The micro-Doppler effect in radar", Artech house, 2019.

[i.7] ETSI TS 103 789 (V1.1.1): "Short Range Devices (SRD) and Ultra Wide Band (UWB); Radar related parameters and physical test setup for object detection, identification and RCS measurement".

[i.8] Mahafza Bassem R.: "Radar systems analysis and design using MATLAB", Chapman and Hall/CRC, 2005.

[i.9] Gong J., Yan J., Li D., Hu H., Kong D.: "Using a Pair of Different-Sized Spheres to Calibrate Radar Data in the Microwave Anechoic Chamber", Applied Sciences. 5 September 2022, 12(17):8901.

[i.10] C. Uluisik, G. Cakir, M. Cakir and L. Sevgi: "Radar Cross Section (RCS) modelling and simulation, part 1: a tutorial review of definitions, strategies, and canonical examples", in IEEE™ Antennas and Propagation Magazine, vol. 50, no. 1, pp. 115-126, February 2008.

[i.11] K. Guan et al.: "On the Influence of Scattering From Traffic Signs in Vehicle-to-X Communications", in IEEE™ Transactions on Vehicular Technology, vol. 65, no. 8, pp. 5835-5849, August 2016, doi: 10.1109/TVT.2015.2476335..

[i.12] L. R. Danoon and A. K. Brown: "Modelling Methodology for Computing the Radar Cross Section and Doppler Signature of Wind Farms", in IEEE™ Transactions on Antennas and Propagation, vol. 61, no. 10, pp. 5166-5174, October 2013, doi: 10.1109/TAP.2013.2272454.

[i.13] R. E. Kell: "On the derivation of bistatic RCS from monostatic measurements", in Proceedings of the IEEE™, vol. 53, no. 8, pp. 983-988, August 1965, doi: 10.1109/PROC.1965.4077.

[i.14] M. Borgese, S. Genovesi, G. Manara and F. Costa: "Radar Cross Section of Chipless RFID Tags and BER Performance", in IEEE™ Transactions on Antennas and Propagation, vol. 69, no. 5, pp. 2877-2886, May 2021, doi: 10.1109/TAP.2020.3037800.

[i.15] ETSI GR ISC 001: "Integrated Sensing And Communications (ISAC); Use Cases and Deployment Scenarios".

[i.16] ETSI GR ISC 003: "Integrated Sensing And Communications (ISAC); System and RAN Architectures".

[i.17] ETSI GR ISC 004: "Integrated Sensing And Communications (ISAC); Security, Privacy, Trustworthiness and Sustainability".

[i.18] "Channel Measurements and Modelling for Joint/Integrated Communication and Sensing, as well as 7-24 GHz Communication", Next G Alliance, July 2024.

[i.19] ETSI GR RIS 003: "Reconfigurable Intelligent Surfaces (RIS); Communication Models, Channel Models, Channel Estimation and Evaluation Methodology".

[i.20] ETSI GR RIS 006: "Reconfigurable Intelligent Surfaces (RIS); Multi-functional Reconfigurable Intelligent Surfaces (RIS): Modelling, Optimization, and Operation".

[i.21] ETSI GR RIS 007: "Reconfigurable Intelligent Surfaces (RIS); Near-field Channel Modeling and Mechanics".

[i.22] Y. Miao et al.: "Dual-band mmWave measurements of human body scattering and blockage effects using distributed beamforming for ISAC applications", European Conference on Antennas and Propagation (EuCAP), 2024.

[i.23] H. C. A. et al.: "Modelling Micro-Doppler Signature of Drone Propellers in Distributed ISAC", IEEE™ Radar Conference (RadarConf24), Denver, CO, USA.

[i.24] J. Chuang et al.: "Quasi-deterministic channel propagation model for human sensing: Gesture recognition use case", IEEE™ Open Journal of Antennas and Propagation, vol. 5(3), pp. 557-572, 2024.

[i.25] A. Ziganshin et al.: "A Scalable Hybrid Channel Model for ISAC Evaluation", International Conference on Microwaves for Intelligent Mobility, 2024.

[i.26] V. C. Chen, F. Li, S. S. Ho and H. Wechsler: "Micro-Doppler effect in radar: phenomenon, model, and simulation study", in IEEE™ Transactions on Aerospace and Electronic Systems, vol. 42, no. 1, pp. 2-21, January 2006.

[i.27] Passafiume M., Rojhani N., Collodi G., Cidronali A.: "Modelling Small UAV Micro-Doppler Signature Using Millimeter-Wave FMCW Radar", Electronics 2021.

[i.28] Huang et al.: "MAJoRCom: A Dual-Function Radar Communication System Using Index Modulation", IEEE™ Trans. Signal Proc., vol. 68, no. 5, pp. 3423-3438, May 2020.

[i.29] P. Kumari et al.: "IEEE 802.11ad-Based Radar: An Approach to Joint Vehicular Communication-Radar System", IEEE™ Transactions on Vehicular Technology, vol. 67, no. 4, pp. 3012-3027, April 2018.

[i.30] Z. Cheng et al.: "Transmit Sequence Design for Dual-Function Radar-Communication System With One-Bit DACs", IEEE™ Transactions on Wireless Communications, vol. 20, no. 9, pp. 5846-5860, September 2021.

[i.31] F. Liu et al.: "Radar-Assisted Predictive Beamforming for Vehicular Links: Communication Served by Sensing", IEEE™ Transactions on Wireless Communications, vol. 19, no. 11, pp. 7704-7719, November 2020.

[i.32] Rahman et al.: "Joint Communication and Radar Sensing in 5G Mobile Network by Compressive Sensing", IET Communications, vol. 14, pp. 3977-3988, December 2020.

[i.33] Kumari et al.: "JCR70: A Low-Complexity Millimeter-Wave Proof-of-Concept Platform for a Fully-Digital SIMO Joint Communication-Radar", IEEE™ Open J. Vehic. Tech., vol. 2, pp. 218-234, March 2021.

[i.34] C. Baquero Barneto et al.: "Millimeter-Wave Mobile Sensing and Environment Mapping: Models, Algorithms and Validation", IEEE™ Trans. Vehic. Tech., vol. 71, no. 4, pp. 3900-3916, April 2022.

[i.35] A. Ali et al.: "Leveraging Sensing at the Infrastructure for mmWave Communication", IEEE™ Communications Magazine, vol. 58, no. 7, pp. 84-89, July 2020.

[i.36] D. He, B. Ai, K. Guan et al.: "The Design and Applications of High-Performance Ray-Tracing Simulation Platform for 5G and Beyond Wireless Communications: A Tutorial", IEEE™ Communications Surveys & Tutorials, vol. 21, no. 1, pp. 10-27, 2019.

[i.37] D. He, K. Guan, D. Yan et al.: "Physics and AI-based digital twin of multi-spectrum propagation characteristics for communication and sensing in 6G and beyond", IEEE™ Journal on Selected in Communications, vol. 41, no. 11, pp. 3461-3473, 2023.

[i.38] A. S. Glassner, Ed.: "An Introduction to Ray Tracing", London, U.K., Academic Press, 1989.

[i.39] V. Degli-Esposti, F. Fuschini, E. M. Vitucci and G. Falciasecca: "Measurement and modelling of scattering from buildings", IEEE™ Trans. Antennas Propag., vol. 55, no. 1, pp. 143-153, January 2007.

[i.40] 3GPP TR 22.837: "Study on Integrated Sensing and Communication".

[i.41] 3GPP TS 22.137: "Integrated Sensing and Communication".

[i.42] Recommendation ITU-R P. 838-3 (2005): "Specific attenuation model for rain for use in prediction methods".

[i.43] Recommendation ITU-R P. 530-18 (2022): "Propagation data and prediction methods required for the design of terrestrial line-of-sight systems".

[i.44] A. A. H. Budalal et al.: "Modification of distance factor in rain attenuation prediction for short-range millimeter-wave links", IEEE™ Antennas and Wireless Propagation Letters, vol. 19, no. 6, pp. 1027-1031, 2020.

[i.45] H. Park, J. Choi, H. Bae et al.: "Measurement and statistics of rain attenuation on terrestrial link at 240, 270 and 300 GHz", 2023 53rd European Microwave Conference (EuMC), pp. 706-709, 2023. .

[i.46] P. Valtr and P. Pecha.: "On distance factor in rain attenuation predictions", Proceedings 13th European Conference on Antennas and Propagation (EuCAP), pp. 1-3, 2019.

[i.47] L. Luini, G. Roveda, M. Zaffaroni et al.: "The impact of rain on short E -Band radio links for 5G mobile systems: Experimental results and prediction models", IEEE™ Transactions on Antennas and Propagation, vol. 68, no. 4, pp. 3124-3134, 2020.

[i.48] 3GPP RP-242348: "Study on channel modelling for Integrated Sensing And Communication (ISAC) for NR".

[i.49] 3GPP SP-231754: "New SID on Study on Architecture Enhancement to support Integrated Sensing and Communication".

[i.50] ETSI TS 122 261: "5G; Service requirements for the 5G system (3GPP TS 22.261)".

[i.51] 3GPP SP-241391: "New Study on 6G Use Cases and Service Requirements".

[i.52] 3GPP TR 22.870: "Study on 6G Use Cases and Service Requirements; Stage 1".

[i.53] 3GPP SP-250833: "Revised SID on Study on Stage 2 for Integrated Sensing and Communication".

[i.54] 3GPP RP-251861: "New SID: Study on Integrated Sensing And Communication (ISAC) for NR".

[i.55] 3GPP RP-251567: "Introduction of Rel-19 channel model for ISAC".

[i.56] "Time-Harmonic Electromagnetic Fields", vol. 9, New York: McGraw Hill, 1961.

[i.57] ETSI TR 138 901 (V19.0.0): "5G; Study on channel model for frequencies from 0.5 to 100 GHz (3GPP TR 38.901 version 19.0.0 Release 19)".

[i.58] Next G Alliance Report Phase II: "Channel Measurements and Modeling for Joint/Integrated Communication and Sensing, as well as 7-24 GHz Communication" 2025.

[i.59] Recommendation ITU-R P. 837-7 (2017): "Characteristics of precipitation for propagation modelling".

3 Definition of terms, symbols and abbreviations

3.1 Terms

Void.

3.2 Symbols

For the purposes of the present document, the following symbols apply

MHz	MegaHertz
mmWave	Millimetre-Wave
THz	Terahertz

3.3 Abbreviations

For the purposes of the present document, the following abbreviations apply:

3GPP	3rd Generation Partnership Project
5G	5th Generation
5GA	5G-Advanced6G 6th Generation
ABG	Alpha-Beta-Gamma
AGV	Automated Guided Vehicle
AoA	Azimuth angle of Arrival
AoD	Azimuth angle of Departure
AS	Angular Spread
ASA	Azimuth angle Spread of Arrival
ASD	Azimuth angle Spread of Departure
ATIS	Alliance for Telecommunications Industry Solutions
BIRA	BIstatic RAdar measurement facility
BS	Base Station
CDL	Clustered Delay Line
CN	Core Network
CSI	Channel State Information
CST	Computer Simulation Technology
CTF	Channel Transfer Function

CW	Continuous Wave
DAC	Data Acquisition Card
DDHC	Data-Driven Hybrid Channel
DGR	Draft Group Report
DS	Delay Spread
EM	ElectroMagnetic
EO	Environment Object
FFT	Fast Fourier Transform
FR1	FRequency 1
FR2	FRequency 2
FR3	FRequency 3
GCS	Global Coordinate System
gNB	5G Node B
GPS	Global Positioning System
IEEE	Institute of Electrical and Electronics Engineers
ISAC	Integrated Sensing And Communications
ITU-R	International Telecommunication Union Radiocommunication
LoS	Line of Sight
LSP	Large-Scale Parameters
MBET	Monostatic-to-Bistatic-Equivalent Theorem
ME	Mean Error
METIS	Mobile and wireless communications enablers for the Twenty-twenty Information Society
MPC	MultiPath Components
NGA	Next G Alliance
NLoS	Non-Line of Sight
NR	New Radio
OFDM	Orthogonal Frequency Division Multiplexing
PCA	Principal Component Analysis
PDP	Power Delay Profile
PEC	Perfectly Electrically Conducting
PL	Path Loss
PRI	Pulse Repetition Interval
RAN	Radio Access Network
RAN1	Radio Access Network working group 1
RCS	Radar Cross Section
RMa	Rural Macrocell
RF	Radio Frequency
RFPA	Radio Frequency Power Amplifier
RIS	Reconfigurable Intelligent Surface
RMSE	Root Mean Square Error
RT	Ray Tracing
RX	Receive
SA	Service and system Aspects
SA1	SA working group 1
SA2	SA working group 2
SF	Sensing Function
SNR	Signal to Noise Ratio
SSP	Small-Scale Parameters
ST	Sensing Target
SVM	Support Vector Machine
TR	Technical Report
TRP	Transmission and Reception Point
TS	Technical Specification
TSG	Technical Specification Group
TU	Technische Universität
TX	Transmit
UAV	Unmanned Aerial Vehicle
UC	Use case
UE	User Equipment
UMi	Urban Microcell
UMa	Urban macrocell

USRP	Universal Software Radio Peripheral
V2I	Vehicle to Infrastructure
V2V	Vehicle to Vehicle
V2X	Vehicle to Everything
WG	Working Group
WP5D	Working Party 5D
XPR	Cross Polarization Ratio
ZoA	Zenith angle of Arrival
ZoD	Zenith angle of Departure
ZSA	Zenith angle Spread of Arrival
ZSD	Zenith angle Spread of Departure

4 State-of-the-art ISAC channel modelling approaches

4.0 General

In this clause, ISAC channel models from the current state-of-the-art are reviewed and summarized, including those from the academic literature, IEEE 802.11bf [i.1], and ETSI TR 138 901 [i.2].

4.1 Related academic research

Several academic papers have been reviewed and their key assumptions for ISAC channel modelling are summarized as follows:

- "MAJoRCom: A Dual-Function Radar Communication System Using Index Modulation" [i.28]:
  - A simple multi-path model is used.
  - 1,9 GHz carrier is assumed.
- "IEEE 802.11ad-Based Radar: An Approach to Joint Vehicular Communication-Radar System" [i.29]:
  - A simple Ricean channel model is used. LoS path is generated based on UE's location, but NLoS path is generated based on random gaussian distribution.
  - Channel gain is generated based on Radar Cross Section (RCS). Radar range will decrease substantially for targets with low RCS (e.g. a pedestrian).
  - Free space pathloss exponent 2 is used.
  - 60 GHz unlicensed band is used.
- "Transmit Sequence Design for Dual-Function Radar-Communication System With One-Bit DACs" [i.30]:
  - A simple LoS path based model. "Swerling-II" model was used, i.e. it is assumed to be constant during each pulse duration but varying from pulse to pulse.
- "Radar-Assisted Predictive Beamforming for Vehicular Links: Communication Served by Sensing" [i.31]:
  - The reflection coefficient (related to the generation of channel gain) is generated based on RCS.
  - 30 GHz carrier frequency is used.
- "Joint Communication and Radar Sensing in 5G Mobile Network by Compressive Sensing" [i.32]:
  - Manual cluster-based model: 3 clusters, AoA centre, moving speeds are randomly generated. In each cluster, random rays are generated.
  - 100 MHz bandwidth is used.

- "JCR70: A Low-Complexity Millimeter-Wave Proof-of-Concept Platform for a Fully-Digital SIMO Joint Communication-Radar" [i.33]:
  - Cluster Delay Line (CDL) model.
  - RCS is used to generate reflection coefficients. 5 dBsm and 8 dBsm (dB relative to square metres) are used.
  - 70 GHz carrier frequency is used.
- "Millimeter-Wave Mobile Sensing and Environment Mapping: Models, Algorithms and Validation" [i.34]:
  - Ray tracing-based model.
  - Subcarrier specific lambda, Far-field assumption.
  - mmWave.
- "Leveraging Sensing at the Infrastructure for mmWave Communication" [i.35]:
  - Ray tracing-based model.
  - mmwave.

There is a rich literature on channel models for ISAC, including the above papers, covering:

- Lack of subTHz sensing channel modelling: the above papers discuss mmWave, radar frequency (e.g. 70 GHz), or lower frequencies (FR1). There is a lack of publications for THz sensing channel measurement.
- RCS is used for sensing cluster channel gain generation:
  - The reflection coefficient is related to the RCS.
- Ray tracing is used to generate target-related rays/clusters generation.
- There is no consideration of the relationship with a communication channel.

4.2 IEEE 802.11bf

In IEEE 802.11bf [i.1], the Data-Driven Hybrid Channel (DDHC) Model is used to support the modelling of sensing uncertainty. The DDHC Model is built based on two parts, a ray tracing method to model target-related rays, and an autoregressive statistical method to model target-unrelated rays. The target-unrelated rays are defined as the rays reflected from fixed objects and perturbed scatters; the target-related rays are defined as the rays reflected from the moving targets. By using a real dataset collected from experiments or ray tracing, the final DDHC Model can be obtained to better approximate the real channel model in a specific scenario. Here is the summary of IEEE 802.11bf [i.1] sensing channel modelling:

- Data driven hybrid channel model is used:
  - Target related rays are generated based on ray tracing:
    - Ray tracing-based model is used:
      - Define a living room scenario
  - Target unrelated rays are generated by an autoregression model and the 11ax/11ay channel model:
    - The target-unrelated rays are generated, by combining the autoregressive model and the channel model in 11ax (for sub 7 GHz) or 11ay (for 60 GHz). The auto-regressive model is given in equation (4.2-1):

$$\vartheta_i(t) = \begin{cases} \gamma(t) & 0 \le t \le T_0 \\ \rho\vartheta_i(t - T_0) + (1 - \rho)\gamma(t) & t > T_0 \end{cases} \quad (4.2\text{-}1)$$

- For 11ax:

$$\gamma(t) = \sum_{n=1}^{N} \sqrt{PL_n} \times \left[\sum_{m=1}^{M} a_{n,m} e^{j\emptyset_{n,m}} \delta\left(t - \tau_{n.m}^{ray}\right)\right] \quad (4.2\text{-}2)$$

- for 11ay:

$$\gamma(t) = \sum_{i=0}^{N_{rays}-1} \left(A^{(i)} U_i^{ch} \left(V_i^{ch}\right)^H \delta(t - t_i)\right) \quad (4.2\text{-}3)$$

- Where ϑ_i is the target-unrelated rays, γ is the 11ax/ay channel model, and T_0 and ρ are the coherent time hyper-parameters, respectively. In equation (4.2-2), N is the number of clusters, M is the number of rays in each cluster, PL_n is the pathloss of the n^{th} cluster, $a_{n,m}$ is the amplitude of the m^{th} ray in the n^{th} cluster, $\tau_{n,m}$ is the time delay of the m^{th} ray in the n^{th} cluster, $\emptyset_{n,m}$ is the phase of the m^{th} ray in the n^{th} cluster. In equation (4.2-3), N_{rays} is the total number of rays, A_i is the amplitude of the i^{th} ray, U_i^{ch} and V_i^{ch} are the channel phasor vectors of the i^{th} ray, t_i is the time delay of the i^{th} ray.

4.3 3GPP

4.3.1 Existing Channel Models (ETSI TR 138 901)

The 3GPP channel model before Rel-19 [i.2] supports both a stochastic model and a model that is a hybrid of a deterministic modelling (ray-tracing) and a stochastic modelling. It is designed for base station to UE communication link (and vice versa) and supports both link level and system level simulations but lacks the sensing channel model aspects. The model is parameterized for a set of communication scenarios. Various sensing scenarios such as monostatic sensing or bistatic sensing channels are not modelled which makes it unsuitable for future sensing use cases. The target modelling requirements are generally dependent on the particular Use Cases (UCs) and underlying performance requirements. In particular, the following aspects can be identified as needing an update to support sensing:

1) Support for mono-static and bi-static sensing: Depending on the device that transmits and/or receives sensing signals, mono-static sensing and bi-static sensing scenarios are considered. For mono-static sensing, mono-static gNB sensing and mono-static UE sensing need to be supported. For bi-static sensing, bi-static gNB-to-UE (or UE-to-gNB) sensing, bi-static UE-to-UE sensing and bi-static gNB-to-gNB sensing need to be supported. For each of these sensing scenarios, Large-Scale Parameters (LSPs) and Small-Scale Parameters (SSPs) additionally need to be defined for sensing channel generation. Depending on the type of target to be sensed and the use case, the altitude, RCS, LSP/SSP generation method, etc., of the target or device may be different.

2) LoS/NLoS state determination for sensing channel: In most radar-based sensing channel modelling, it is assumed that a target exists (i.e. the channel between the target and the sensing device is LoS state). This may be sufficient for evaluating only sensing performance, but to evaluate performance from a system perspective and evaluate integrated sensing and communication performance, an actual channel model including both LoS and NLoS between the sensing device and target is needed. The existing distance-dependent LoS/NLoS state decision probability model may be reused (in this case, the distance between the Tx device and the Rx device should be replaced with the distance between the Tx sensing device and the target and the distance between the target and the Rx sensing device), or based on measurement or channel sounding, and new models for sensing LoS/NLoS state determination may be discussed. Additionally, parameters such as Delay Spread (DS), Angular Spread (AS), shadowing factor, Path Loss (PL), etc. may be determined differently depending on the LoS/NLoS state.

3) Large Scale Parameters (LSPs) for sensing channel: DS, AS, SF, PL, and Ricean K factor (K) can be different from those of the communication channel. In a communication channel, since the base station and the UE have different antenna heights, it is desirable to use different angular distributions for AoA and AoD. However, in the case of mono-static sensing, since the Tx and Rx are co-located and their antenna height are the same, the AoA and AoD could have the same distribution.

4) Small Scale Parameters (SSPs) for sensing channel: This can be classified into the cluster/Ray modelling for the sensing channel and the effect of mobility:

   a) Cluster/Ray modelling for sensing channel: Deterministic or semi-deterministic Ray/Cluster modelling can be considered. With deterministic modelling the location of the cluster is determined based on the physical location and characteristics of the object (target or clutter) while semi-deterministic may model the characteristics of the object stochastically. Delay, gain, and echo angle for a direct path toward a sensing target are determined based on the physical location of a sensing target. Delays, gains, and angles for indirect paths toward the sensing target are generated in a statistical manner based on measurement or sounding results. If the target is located very close to the sensing device, the near-field effect can also be considered. This may be seen as generating channels that include a single bounce toward/from the target and channels that have multi-bounces toward/from the target. If the sensing target creates one or more clusters and multiple rays exist within the one or more clusters, one of the rays corresponds to a direct path and the rest of the rays correspond to indirect paths. Based on these rays, a multi-path channel can be generated for a sensing target. There is also a need to discuss how the delay and angle of the background channel are generated. The channels generated by the surrounding environment or clutter can be distinguished from channels generated by targets. There is a need to further discuss how to generate clusters/rays generation for mono-static sensing and bi-static sensing. When implementing a cluster for a sensing object, it is needed to discuss whether to generate a cluster for the sensing object in addition to the existing communication clusters or assign one or more clusters from the generated clusters for communication with the sensing object.

   b) Effect of mobility: The device mobility is already modelled in communication channel modelling, but target mobility also needs to be considered.

5) Target Modelling:

   a) RCS consideration: RCS needs to be characterized for the relevant sensing targets/scenarios:

      i) Different sensing targets such as humans, vehicles, or AGV/AMR (smart factory) may have different RCS values and human health signals (respiration/heartbeat channel signatures) may have different modelling approaches e.g. using micro-Doppler modelling or variational RCS values.

      ii) The channel modelling supports different related deployment scenarios (e.g. RCS characterization for various Tx/Rx position with respect to the sensing target).

      iii) For use cases involving target identification, posture recognition, orientation detection, etc., the geometry of sensing targets should be modelled. Instead of a single RCS value, the scattering field of a target can be model by multiple scattering centres with given relative locations and different RCS models. The expanded multi-scattering centre uses multiple scattering points to abstractly describe the electromagnetic scattering characteristics of the target, which can more accurately restore the amplitude and the shape information of the target.

      iv) It should be discussed if the RCS is modelled as part of the large-scale parameters in the path loss or is modelled as part of the small-scale parameters on a target's ray/cluster.

6) XPR for sensing channel: In mono-static sensing, even if the channel between the sensing device and the target is LoS, the channel itself should be modelled for reflected wave. Note that in a communication channel, an infinite XPR value is used for the LoS path (i.e. a diagonal matrix is used for an X-pol channel generation), but in a sensing channel, an XPR value of infinity should not be used for the direct path toward the sensing target, and the mean and variance of XPR may be different from those of communication channel. For bi-static sensing, it is possible to reuse XPR values for communication channels.

7) Consistency: Some use cases may require spatial/temporal consistency modelling. For example, it is assumed a case where multiple devices cooperate to sense a single target. If the sensing channels of the two devices are generated independently, the cooperative sensing performance may be incorrectly estimated. If two devices are physically close together or a device or a target moves in limited space, their channel generation may also correlate. It is necessary to discuss to make a correlation in LSPs and/or SSPs generation between spatial/temporal displacements.

8) Background channel consideration: The interaction between the background environment and sensing targets can be important for sensing performance evaluation. The reflections from the environment object not just from the sensing target can take a large portion in the received power, which contains explicit geometry information between sensing target, Tx, Rx, and other environmental objects. For example, the reflection paths can be exploited to create a virtual TRP to improve the localization accuracy for target localization and tracking. The major objects, such as buildings in the scenarios, are considered environment objects. The interaction between the sensing target and environmental objects and the interaction between environmental objects need to be modelled.

9) Frequency range limitation for sensing: ETSI TR 138 901 [i.2] model has a limitation of frequency range up to 100 GHz. For sensing use cases, this may also need to be extended e.g. to THz bands or validated in a new band e.g. FR3.

Based on the above analysis, the limitations of channel modelling before Rel-19 in ETSI TR 138 901 [i.2] for ISAC are summarized:

1) Support for mono-static and bi-static sensing.

2) LoS/NLoS state determination for sensing channel.

3) Large Scale Parameters (LSPs) for sensing channel.

4) Small Scale Parameters (SSPs) for sensing channel:

   a) Cluster/Ray modelling for sensing channel.

   b) Effect of mobility.

5) Target Modelling: RCS consideration.

6) XPR for sensing channel.

7) Spatial consistency.

8) Environment channel consideration.

9) Frequency range limitation for sensing.

4.3.2 SA1/SA2

3GPP TR 22.837 [i.40] (SA1) identified and studied 32 use cases for integrated sensing and communication, as well as the potential requirements for enhancing the 5G system to provide sensing services. The normative functional and performance requirements for 5G wireless sensing services were detailed in 3GPP TS 22.137 [i.41] and ETSI TS 122 261 [i.50].

Although there is currently no ongoing work dedicated for ISAC in 5GS in SA1, a new study item to explore 6G use cases and requirements was approved in [i.51], and the agreed new use cases with proposed 6G ISAC requirements are captured in 3GPP TR 22.870 [i.52]. The ISAC service requirements for 5GS from [i.41] are taken as a baseline for potential 6G ISAC service requirements.

At the commencement of the present document, 3GPP TSG SA2 had an endorsed Study Item in [i.49] on ISAC architecture, on hold. An updated Study item in [i.53] to study ISAC Architecture in 5GS for gNB based mono-static sensing for UAV use case, aligned with a new RAN1 led 5GA ISAC study on performance evaluation and RAN and CN signalling procedures in [i.54], were both approved at their respective 3GPP TSG SA and RAN Plenary meetings #108 in June 2025.

The aligned SA2 work scope focuses on Architecture, functional enhancements and operational procedures to support gNB mono-static sensing for UAV services, in line with the SA1 requirements captured in [i.41]. The scope proposes to focus on a sub-set of use cases e.g. commercial, automotive, public safety and emergency services.

4.3.3 RAN1

3GPP RAN1 has conducted a study in parallel to the present document to define a channel model [i.48] to support a subset of Integrated Sensing and Communication use cases and related requirements captured in 3GPP TS 22.137 [i.41].

Specifically the study aimed to capture a common channel modelling framework capable of detecting and/or tracking the following objects and distinguishing them from unintended objects:

- UAVs.
- Humans indoors and outdoors.
- Automotive vehicles (at least outdoors).
- Automated guided vehicles (e.g. in indoor factories).
- Objects creating hazards on roads/railways, with a minimum size dependent on frequency.

The study included all six sensing modes (i.e. TRP-TRP bistatic, TRP monostatic, TRP-UE bistatic, UE-TRP bistatic, UE-UE bistatic, UE monostatic) and focused on the frequency range 0,5 GHz to 52,6 GHz with the assumption that the modelling should scale to 100 GHz.

Enhancements to the stochastic model from ETSI TR 138 901 [i.2], with consideration of known characteristics of physical objects were prioritized in the study as opposed to other models e.g. map based hybrid channel or ray-tracing models. The resulting output of this RAN1 study to support sensing in ETSI TR 138 901 [i.2] was approved in 3GPP RP-251567 [i.55], in RAN#108 in June 2025.

The reference communication scenarios for each target type (object) are basically reused and these are to be used to obtain scenario parameters to define the properties of the sensing Tx/Rx and target.

The channel modelling framework includes:

- The ISAC channel is composed of a component of target channel and a component of background channel.
- Multiple sensing targets can be modelled in the ISAC channel of a pair of Tx and Rx.
- The same sensing target can be modelled in the ISAC channels of multiple pairs of Tx and Rx.
- NLoS components in target channel can be modelled by stochastic clusters or Environment Objects (EOs):
  - EO type-1 having same/similar model as a sensing target.
  - EO type-2 (e.g. ground, wall, ceiling) modelled by specular reflection.

For the Target channel, it includes:

- For each Tx-target link/target-Rx link, the LoS state could be LoS or NLoS.
- Generated by concatenation of parameters of Tx-target link and target-Rx link.
- A ST is modelled with one or multiple scattering points. Each scattering point of a ST is used to model the total scattering effects of some adjacent scattering centres at the ST. The impact of a single scattering point to the channel includes at least two aspects, i.e. the Radar Cross Section (RCS) and the polarization matrix.
- The RCS related coefficient of a single scattering point for a pair of incident/scattered angles is composed of a first component which is included in the large-scale parameters, and a second component and a third component which are both included in the small-scale parameters. The patterns and values for each component for different sensing targets are provided.

It allows the reuse of existing channel model from ETSI TR 138 901 [i.2] in each of the Tx-target link and the target-Rx link.

And for the Background channel, it includes:

- For TRP-UE, UE-TRP bistatic sensing mode, procedures in the existing ETSI TR 138 901 [i.2] is reused.
- For TRP and UE mono-static sensing mode, 3 reference points are generated following Gamma distribution, and then the procedures in the existing ETSI TR 138 901 [i.2] are reused between the real sensing Tx and each reference points.

On conclusion of this Channel Modelling study RAN1 has started a follow up study item [i.54], aligned with SA2, to study performance evaluation and related RAN and CN signalling procedures for the gNB-mon-static sensing for the UAV use cases.

4.4 Other forums review

4.4.1 ATIS Next G Alliance

ATIS NGA has completed its Phase 1 activity, looking at channel modelling and propagation measurements, with the current status of ISAC measurement data, see White Paper in [i.18]. The Phase 2 report [i.58] extends the efforts by offering additional measurements for communication channels within the 7 - 24 GHz range and sensing channel models that encompass both targets and environmental settings. The measurements include RCS characterization of targets such as vehicles, drones, humans, and robotic arms, demonstrating that a unified RCS modeling framework can be adapted to a variety of ISAC targets. Also, the group has made a submission to ITU-R WP5D meeting #47 on test environments for sensing.

4.4.2 ETSI ISG RIS

Reconfigurable Intelligent Surface (RIS) is a new type of network node that can be controlled and configured to improve communication performance, positioning, and sensing capabilities. ETSI ISG RIS has studied several aspects related to deployment of RIS in existing and upcoming wireless technologies and networks, including 6G ISAC. In particular, ETSI GR RIS 003 [i.19] provides detailed channel models and evaluation frameworks for RIS-integrated systems. including for RIS-based ISAC systems. Signal and channel modelling for multi-functional RIS, including those with sensing capability, is studied in ETSI GR RIS 006 [i.20]. The group is working on further modelling for near-field RIS, including for sensing applications, in ETSI GR RIS 007 [i.21].

4.4.3 ETSI ISG THz

ETSI ISG THz has conducted measurements and developed path loss models from 90 GHz to 300 GHz in different deployment scenarios indoor and outdoor primarily in Line of Sight (LoS). Non-Line of Sight (NLoS) measurements have been performed in single frequency or two frequency bands which did not enable the development of the ABG path loss model due to the limited power and dynamic range available at the higher frequency band above 170 GHz. The measurements were wideband and can be used to estimate the channel parameters for system design such as rms delay spread. Other propagation studies include human blockage, large arrays and near-field propagation effects, and impact of molecular absorption. Human blockage measurements were performed both using CW and wideband, and compared with standard models including METIS and ITU-R models.

4.4.4 INTERACT Cost Action

In COST Interact WG 2 there is a sub working group on ISAC.

In general, most use cases studied are on infrastructure-based sensing (vehicles, UAV, human), V2X, industrial, Indoor sensing, and gesture recognition for communication centric systems like 5G or Wi-Fi®.

Channel Modelling and Measurements:

1) V2I Radio Channel Triband Measurements:
   - Frequency bands:
     - 3,2 GHz;
     - 34,3 GHz;
     - 62,35 GHz.
2) 28 GHz ISAC Vehicular Channel Measurements/Modelling.

3) Indoor Dual-Band Beamforming Channel Measurements (mmWave):
   - Sensing technologies:
     - 5G NR; or
     - WiGig.
   - Frequency bands:
     - 24 GHz;
     - 60 GHz.
4) Human Body Scattering and Blockage Effects Using Distributed Beamforming for ISAC Applications [i.22].
5) Bistatic Radar measurement facility (BIRA):
   - Bandwidth:
     - 4 GHz.
   - Frequency range:
     - FR1; and
     - FR2 (up to 170 GHz).
6) RCS + Micro-Doppler Modelling.

EXAMPLE: Drone propeller micro-Doppler signature [i.23].

7) Gesture Recognition and Quasi-Deterministic Channel Propagation Model [i.24]:
   - Frequency band:
     - 28 GHz.
8) Physics-Informed Generative Neural Networks for RF Propagation Prediction.
9) Hybrid Channel Model for ISAC Simulation Framework [i.25].
10) UAV/Vehicle-Based Channel Measurement Campaign (sub-6 GHz):
    - Measurement setup:
      - UAVs/vehicles as targets, static/dynamic Tx/Rx.
    - Location:
      - TU Ilmenau.

4.4.5 ITU-R

The International Telecommunication Union Radiocommunication Sector (ITU-R) develops a wide range of global standards for the use and management of radiocommunication systems. It has established a systematic framework for studying rain attenuation. It provides methods for estimating signal loss in communication systems caused by rain, which is essential for accurately predicting the performance of wireless communication links in rainy weather. This framework is primarily based on the prediction models outlined in Recommendations ITU-R P.530-18 [i.43] and P.837-7 [i.59], which assess the effects of signal attenuation by incorporating parameters such as rainfall rate, frequency, polarization mode, and path length. Recent research has concentrated on refining the modelling of rain attenuation characteristics at high frequency bands, combining satellite remote sensing and ground meteorological data to enhance regional applicability. Additionally, in response to the requirements of millimeter-wave communication and the deployment of 5G/6G networks, the ITU-R is promoting research on multi-scenario composite attenuation models. This research aims to support the design of reliable communication links under extreme weather conditions.

One of the prevalent methods for calculating rain attenuation based on the rain rate is by leveraging the prediction approach put forth in Recommendation ITU-R P.838-3 [i.42]. It encompasses three influential factors: rainfall rate, polarization mode, and frequency, which is expressed as:

$$\gamma_{\mathrm{R}} = kR^{\alpha}, \tag{4.4-1}$$

where γ_R is specific attenuation (dB/km). the parameters k and α are determined as function of frequency f [GHz]:

$$\log_{10} k = \sum_{j=1}^{4}\left\{a_j \exp\left[-\left(\frac{\log_{10} f - b_j}{c_j}\right)^2\right]\right\} + m_k \log_{10} f + c_k, \tag{4.4-2}$$

and

$$\alpha = \sum_{j=1}^{5}\left\{a_j \exp\left[-\left(\frac{log_{10} f - b_j}{c_j}\right)^2\right]\right\} + m_\alpha \log_{10} f + c_\alpha. \tag{4.4-3}$$

Depending on whether the polarization is vertical or horizontal polarization, coefficient k and α are determined as k_{V} or k_{H}, and α_{V} or α_{H}, where V represents vertical polarization and H represents horizontal polarization, and the calculation value varies accordingly. For calculating the coefficients, the detail is in [i.42] including tables for a, b, c and m.

The total attenuation A for a specific distance depends on the effective path length d_{eff}, between the transmitter (Tx) and receiver (Rx) as:

$$A = \gamma_{\mathrm{R}} d_{\mathrm{eff}}, \tag{4.4-4}$$

where the effective path length d_{eff} of the link is obtained by multiplying the actual path length d by a distance factor r.

The Recommendation ITU-R P.530-18 [i.43] model incorporates a distance factor to account for spatial rain rate variations that are not captured by the uniform distribution assumption of the Recommendation ITU-R P.838-3 [i.42] model:

$$r = \frac{1}{0.477 d^{0.633} R_{0.01}^{0.073\alpha} f^{0.123} - 10.579(1-\exp(-0.024d))}. \tag{4.4-5}$$

In [i.44], an in-depth investigation of the distance factor specified in Recommendation ITU-R P.530-18 [i.43] revealed that the distance factor undergoes significant variations for short-range link (less than 1 km).

5 Proposed ISAC channel modelling approaches

5.0 General

In this clause, some advanced approaches for 6G ISAC channel modelling are provided. These advanced features go beyond the approaches described in clause 4, and can be used for performance evaluation and feasibility analysis of future 6G ISAC solutions.

5.1 Use cases, scenarios and frequency bands

ETSI GR ISC 001 [i.15] on ISAC Use Cases and Deployment Scenarios is to identify and describe advanced ISAC use cases and identify key requirements stemming upon future 6G communications systems to support these advanced use cases.

For many of proposed use cases in ETSI GR ISC 001 [i.15], the related approaches of channel modelling described in clause 4 can be used for the potential evaluation. For example, ETSI TR 138 901 (V19.0.0) [i.57] can be used for object detection and/or tracking including UAVs, human indoors and outdoors, AGV, Vehicle, Objects creating hazards on roads/railways, and even environment objects. This channel modelling is valid for most of the use cases, including for the use case of body proximity sensor, airborne-based sensing for environment reconstruction, high-resolution topographical maps, Use case on collaborative robots based on digital twinning, use case on traffic throughput and safety on road intersections, use case on safe & economic UAV transport, use case for automated guided vehicles travelling in airports, use case on emergency vehicle route planning, use case on enhanced network performance and efficient use of resources via sensing-aided communications.

For all use cases, RCS modelling for different types of sensing objects is needed for potential evaluation. For RF sensing, the operating frequency significantly impacts the sensing characteristics, as objects may exhibit varying Radar Cross-Sections (RCSs) across different frequency bands.

Especially, for some use cases, micro-Doppler modelling as described in clause 5 may be further needed to evaluate the human body's small-scale motion, such as human gesture, breathing, heartbeat, etc. This advanced channel modelling part is valid for the use case on human motion recognition, the use case on real-time monitoring of health hazard and disaster risk, the use case on emergency search and rescue, the use case for outdoor healthcare sensing and monitoring, the use case on remotely controlled robots for senior citizen monitoring and care. For the same target velocity, higher frequencies generate larger Doppler or micro-Doppler shifts, improving the ability to detect and differentiate moving objects. Basically, the proposed micro-Doppler ISAC channel modelling is applicable for all frequency bands.

For another use cases, for example, the use case on micro-deformation sensing, Ray Tracing (RT) simulation methodology may be used for specific scenarios, such as bridge micro-deformation.

For use cases in dense vehicular networks, or low-altitude drone operations, precise rain attenuation modelling is required to ensure stable mmWave signal transmission under heavy rainfall, while enabling dynamic optimization of short-range communication links. For those use cases such as airborne-based sensing for environmental reconstruction, on traffic throughput and safety on road intersections, on safe & economic UAV transport, emergency vehicle route planning, etc., the model could enable real-time prediction of dynamic rain attenuation affecting mmWave links.

For some other use cases, for example, the use case on precise localization for robot grasping, the use case of body proximity sensor, near-field modelling for sensing may be needed because the sensing transceiver may have large size of antenna array, and may be very closed to the sensing target.

5.2 RCS Modelling

5.2.1 Definition

In ETSI TS 103 789 [i.7], the Radar Cross Section of a target object was defined as "the cross-sectional area of a perfectly reflecting sphere that would produce the same strength reflection as would the target in question". A more detailed definition is "the measure of a target's ability to reflect a radar signal in the direction of the radar receiver i.e. it is the measure of the ratio of backscatter per steradian in the direction of the radar (from the object) to the power density that is intercepted by the target". Hence, the RCS indicates how detectable the target object is based on the incidence of the electromagnetic waves on its surface. The RCS measurement and modelling is a key element in modelling the ISAC channel in most of these use-case scenarios since different target object categories respond differently to the incidence of electromagnetic field. In this clause, the main requirements for RCS modelling in the ISAC channel are proposed and an initial approach to model different target objects in the environment is outlined.

5.2.2 RCS Model Dependencies

The RCS of a target object is a characteristic feature of the object. Modelling the RCS should take into consideration of the following parameters [i.7], [i.8]:

a) Frequency of the incident radio signal.

b) Angles of incidence and scattering, where the angle of incidence can be defined as the angle between the LoS path (Tx - the target) and the normal to the target surface, the scattering angle can be defined as the angle between the LoS path (Rx - the target) and the normal to the target surface.

c) Polarization of the transmitter and the receiver.

d) Type of the target object:

   i) Target object material.

   ii) Target object size.

   iii) Target object shape.

e) Target object material.

f) Target object size.

g) Target object shape.

h) Target object motion/sub-motion.

i) Target object orientation.

j) Antenna pattern.

k) Temporal or spatial consistency.

l) Distance from Tx or Rx.

5.2.3 RCS Model Boundaries

1) Frequency Region: RCS represents the object electromagnetic signature on the incidence wave. This signature is shaped by the ratio of the target dimension to the incidence radio signal wavelength [i.9] and [i.10]. RCS frequency of operation can be classified into three types according to this ratio:

   a) Low frequency (Rayleigh region) $2\pi l/\lambda \ll 1$.

   b) Medium frequency (Mei Region) where $2\pi l/\lambda \sim 1$.

   c) High frequency, where $2\pi l/\lambda \gg 1$.

   Where l and λ are the maximum object dimension and carrier wavelength, respectively. Most of the RCS models in previous literature assumes the object to operate in the high frequency region.

2) Near-field/Far-Field: RCS modelling assumes the illumination of the target object with plane waves, which is the case in the far-field region. The far-field region condition should be defined with respect to both the Tx/Rx antennas and the object:

   a) Far-field region condition from Tx/Rx antennas: For the object to exist in the far-field region from the Tx/Rx antenna, it should be located at distance r, such that $r > \frac{2{D_{ant}}^2}{\lambda}$, where D_{ant} is the largest dimension of the antenna physical aperture [i.7].

   b) Far-field region condition from the object: To guarantee that also the Tx and Rx are in the far-field region from the object should be located at distance $r > \frac{2{D_{\max}^{\text{obj}}}^2}{\lambda}$, where $D_{\max}^{\text{obj}}$ is the largest object dimension [i.11].

   The effect of the near/far-field on the target RCS should be investigated including the following points:

   a) Effect with respect to the RCS model dependencies.

   b) Effect with respect to the target representative model (e.g. single point vs. multipoint).

3) Monostatic/Bistatic RCS: RCS can be evaluated in either a monostatic or bistatic scenario. Since most of the RCS models and measurements in previous literature were formulated in monostatic scenario, bistatic RCS models can be evaluated using monostatic measurements/models through the Monostatic-to-Bistatic-Equivalent Theorem (MBET) [i.11].

4) Object Shape: In [i.7], the RCS for basic shapes is formulated as in the case of sphere, rectangular sheet, trihedral shape, etc. However, complex shapes do not have general formulas or models. In [i.11], [i.12] and [i.13], complex shapes can be decomposed into basic shapes and the overall RCS of the complex shaped object can be evaluated through combining the RCS equivalent share of its decomposed basic components.

5) Object Material: The RCS changes with the change in the object material. In [i.14], an approximation was presented take into consideration the object material effect in RCS evaluation. The approximation made in [i.14] was through multiplying the RCS of perfect electric conducting equivalent object by the reflectivity of the target object.

5.2.4 RCS Modelling Approaches

The approaches used to model the object RCS can be classified into two main categories:

1) top-down; and

2) bottom-up approaches.

In the top-down approach, the RCS model is generated based on measuring the ratio between the scattered and incident electric fields from the object. The values of the scattered and incident electric fields can be obtained from measurement campaigns, numerical simulations, or ray-tracing tools. The object RCS can be evaluated using the following formula:

$$\sigma = \lim_{R \to \infty} 4\pi R^2 \frac{|E_s|^2}{|E_i|^2} \quad (5.2\text{-}1)$$

where R is the object separation distance from the receiver (i.e. where the scattered power is measured), E_s and E_i are the values of the scattered and incident electric fields, respectively.

For the bottom-up approach, the RCS model is generated through deriving closed forms for both the scattered and incident electric fields using electromagnetic propagation theory. To obtain practical results, bottom-up approach may calibrate the generated RCS model using the obtained results from measurement campaigns or electromagnetic numerical simulations.

Top-down approaches are mainly used to measure the RCS of complex objects like humans, vehicles, etc. However, the main drawback in this case is the limited applicability of the obtained RCS model to the use case under consideration. Bottom-up approaches are mainly used to derive the RCS model of basic objects like rectangular, spherical, dihedral shapes, etc. The main advantage in bottom-up derived models is its scalability to different basic object sizes, frequencies, materials, etc. However, the main drawback of such approach is the difficulty of extending such models to more complex shapes.

5.2.5 Multipoint target modelling

One way to bridge the gap between the two approaches is through multipoint representation for the target. Target object segmentation can be considered as one way of multipoint target representation for RCS modelling, other methods can also be adopted for multipoint target representation. Segmentation aims to divide the complex object into more basic and simpler objects with pre-known RCS. For example, in [i.11], the authors divide the traffic sign into two basic objects cylinder and square shapes to represent the pillar and the traffic sign, respectively. In [i.12], the authors used the segmentation approach to evaluate the RCS of wind turbine blades through decomposing the turbine blade into rectangular segments. Moreover, authors in [i.11] used the segmentation approach to calculate the RCS of objects that have electrically large sizes (i.e. compared to the carrier wavelength), where multiple object reflection points are considered. The evaluated object RCS using segmentation can be further calibrated through either measurement results or electromagnetic numerical simulation tools such CST.

Segmentation approach can be a promising approach in building up an RCS model for complex objects using the pre-known RCS of basic objects. The resulting RCS model can be scalable to accommodate different frequency bands or object dimensions. Also, segmentation can be used to evaluate the RCS of electrically large sized objects at different separation distances from the Tx/Rx. The next clause presents the evaluation approach for the average RCS of a segmented object.

5.2.6 Segmented Object Average RCS

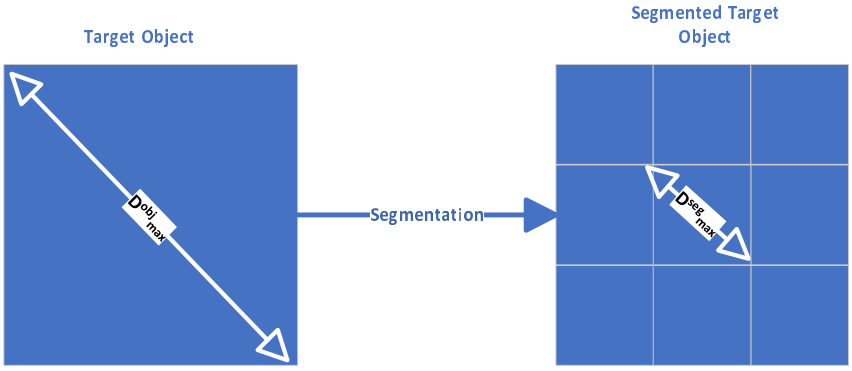

Figure 5.2-1: Object segmentation approach

In Figure 5.2-1, the target object is decomposed into N segments, where each segment has an RCS value of σ_i. σ_i can be evaluated based on the segment shape (circular, rectangular, etc.), dimensions and frequency of operation. The object average RCS σ_{obj} can be computed as:

$$\sigma_{obj} = \left|\sum_{i=1}^{N} \sqrt{\sigma_i} e^{j\varphi_i}\right|^2 \quad (5.2\text{-}2)$$

where N is the number of the object segments and φ_i is the phase difference between the i-th segment and the first segment. It can be calculated as:

$$\varphi_i = k\Delta d_i \quad (5.2\text{-}3)$$

where k is the wave-vector number, and Δd_i is the difference in the signal propagation path length between the i-th segment and the 1st reference segment. It worth mentioning that equation (5.2-3) applies to the line-of-sight case between the target and the Tx/Rx, for the NLoS case other methods should be adopted to calculate the phase difference between the first/reference segment and the other segments of the target.

5.2.7 Number of Object Segments

The target object RCS computation is dependent on whether the incident/scattered electromagnetic wave from the object can be considered as plane wave or not. The incident/scattered wave can be approximated to plane wave if the following condition is satisfied [i.11]:

$$\min\left(r_{\mathrm{tx-obj}}, r_{\mathrm{obj-rx}}\right) > \frac{2(D_{\max}^{\mathrm{obj}})^2}{\lambda} \quad (5.2\text{-}4)$$

where $r_{\mathrm{Tx-obj}}, r_{\mathrm{obj-Rx}}$ are the distances from the transmitter to the object, and from the object to the receiver, respectively. $D_{\max}^{\mathrm{obj}}$ is the maximum object dimension, and λ is the carrier wavelength.

If the above condition is not met, then the plane wave approximation is not valid. In this case, an object segmentation approach is applied. In this approach, the scattering object is segmented into multiple (N) scattering segments, where N should be in the range $[N_{\min}, N_{\max}]$. The minimum number of segments $N_{\min}$ is obtained such that the maximum object segment dimension $D_{\max}^{\mathrm{seg}}$ satisfies the following:

$$\min\left(r_{\mathrm{Tx-seg}}, r_{\mathrm{seg-Rx}}\right) > \frac{2(D_{\max}^{\mathrm{seg}})^2}{\lambda} \quad (5.2\text{-}5)$$

The maximum number of segments $N_{\max}$ is obtained such that $D_{\max}^{\mathrm{seg}}$ satisfies the following condition, ensuring that the segment dimension is greater than the carrier wavelength:

$$\frac{2\pi}{\lambda} D_{\max}^{\mathrm{seg}} \gg 1 \quad (5.2\text{-}5a)$$

5.2.8 RCS fading model

In Figure 5.2-2, the RCS of a metallic plate is evaluated at different aspect angles and separation distances from the sensing receiver. The aspect angle is defined as the average of the incidence and the scattering angles that are measured with respect to the normal to the surface of the plate. The evaluated RCS exhibits a fast-fading performance with rapid change in the aspect angle, which means that the RCS can have a fast fading component with respect to the incidence/scattering angles, i.e. AoA/AoD with respect to the sensing cluster.

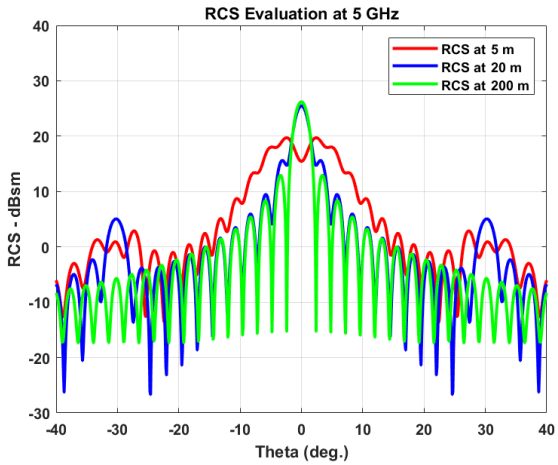

Figure 5.2-2: RCS at different aspect angles and separation distances from the sensing receiver

Consequently, the sensing target $\mathrm{RCS}(\mathrm{dBsm})$ can be divided into two main components as:

$$\mathrm{RCS}(\mathrm{dBsm}) = (10\log10(\mathrm{RCS}^{SF}))(\mathrm{dBsm}) + (10\log10(\mathrm{RCS}^{FF}))(\mathrm{dB}) \quad (5.2\text{-}6)$$

where RCS^{SF} and RCS^{FF} are the slow-fading and fast-fading components of the sensing target RCS. RCS^{SF} is dependent on sensing target related parameters (e.g. shape, size, material, separation distance from Tx/Rx etc.) and part of incident signal parameters (e.g. frequency, polarization, etc.). RCS^{FF} is dependent on the incidence/scattering angle from the sensing target, which can vary with the change of the sensing target orientation with respect to the sensing Tx/Rx. RCS^{FF} can be seen as a model for the RCS directivity gain in a specific direction.

RCS^{FF} can be modelled as the normalized RCS, while the RCS^{SF} is evaluated as the RCS maximum value for each separation distance. Hence, the RCS^{SF} can be evaluated as 19 dBsm, 25 dBsm, 26 dBsm, at separation distances 5 m, 20 m and 200 m, respectively. The RCS^{FF} is demonstrated in Figure 5.2-3.

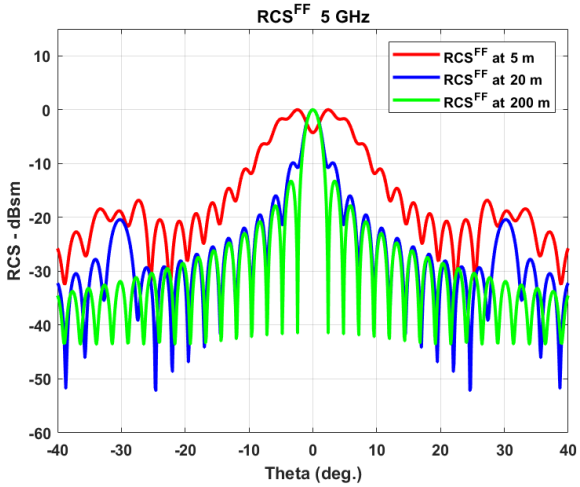

Figure 5.2-3: RCS fast fading component at different aspect angles and separation distances from the sensing receiver

5.2.9 Views on RCS incorporation in ETSI TR 138 901

To incorporate RCS, its slow-fading and fast-fading components (RCS^{SF} and RCS^{FF}) can be included within the channel LSP and SSP procedures.

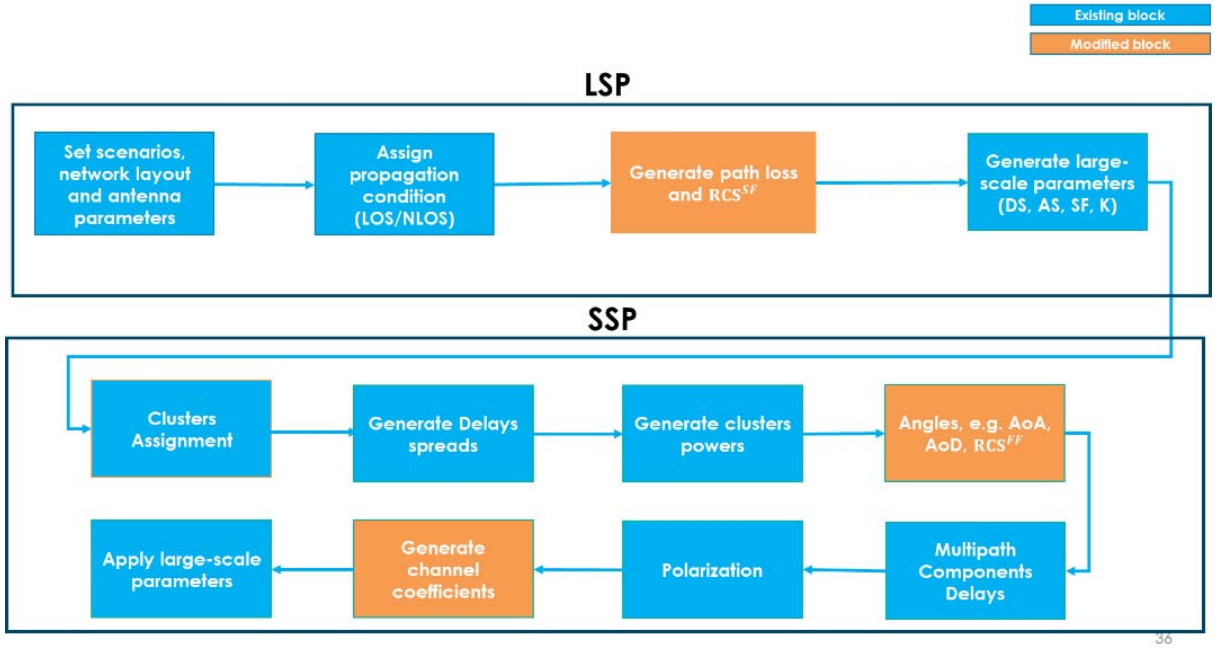

Figure 5.2-4: Modified Blocks in TR38.901 to incorporate the RCS

Figure 5.2-4 highlights the amended blocks to integrate the RCS model with its two components RCS^{SF} and RCS^{FF}. The first amended block is the Path Loss (PL) model to integrate the slow-fading component of the RCS as:

$$\mathrm{PL(dB)} = \mathrm{PL(dB)} - \mathrm{A(dBsm)} \tag{5.2-7}$$

The $\mathrm{PL(dB)}$ is the path loss evaluated based on the signal propagation path distance from the sensing transmitter to the sensing target, then to the sensing receiver, taking into account the propagation scenario and condition (e.g. LoS/NLoS). A can be expressed as $10\log10(\mathrm{RCS}^{SF})$ which represents the slow-fading part of the RCS in dBsm.

The second block to be amended is the cluster angles evaluation, where the evaluation of the fast-fading RCS component RCS^{FF} in this block is proposed to be added. As previously mentioned, the RCS^{FF} is dependent on the incidence and scattering angles from the target. Consequently, RCS^{FF} will have two components based on the azimuth and zenith AoA ($\varphi_{AoA}, \theta_{AoA}$) and AoD ($\varphi_{AoD}, \theta_{AoD}$) to/from the sensing target as: the azimuth component $\mathrm{RCS}^{FF}{}_{\varphi_{AoA},\varphi_{AoD}}(\varphi_{AoA}, \theta_{AoA}, \varphi_{AoD}, \theta_{AoD})$ and the zenith component $\mathrm{RCS}^{FF}{}_{\theta_{AoA},\theta_{AoD}}(\varphi_{AoA}, \theta_{AoA}, \varphi_{AoD}, \theta_{AoD})$.

The last block to be amended is the channel coefficient generation, where the RCS^{FF} two components can be integrated into equations (7.5-28) and (7.5-29) in ETSI TR 138 901 [i.2] in the form of a diagonal matrix as:

$$\begin{bmatrix} \mathrm{RCS}^{FF}{}_{\theta_{AoA},\theta_{AoD}} & 0 \\ 0 & \mathrm{RCS}^{FF}{}_{\varphi_{AoA},\varphi_{AoD}} \end{bmatrix} \tag{5.2-8}$$

5.2.10 Electromagnetic based RCS Modelling

This clause presents an Electromagnetic (EM)-based method for modelling the RCS of targets represented by multiple scattering points. Specifically, each scattering point in this model is represented by a single cylinder. To illustrate this approach, the scattering model of a single cylinder is first analysed, as it serves as the foundation for the overall scattering method. A 2D scattering scenario confined to the horizontal plane is considered, represented in cylindrical coordinates (ρ, φ). A Perfect Electric Conductor (PEC) cylinder of radius a is centred at the origin and a current filament parallel to the cylinder axis is positioned at $\boldsymbol{\rho}_t = (\rho_t, \varphi_t)$. When the filament is an electric current I_t, the incident electric field E_z^i generated by the current filament is derived from cylindrical wave expansions [i.56]:

$$E_z^i = -\frac{\omega\mu_0}{4} I_t H_0^{(2)}(k_0 \|\boldsymbol{\rho} - \boldsymbol{\rho}_t\|) \tag{5.2-9}$$

where $k_0 = \omega\sqrt{\mu_0\epsilon_0}$ denotes free-space wavenumber, with denoting angular frequency, $\mu_0$denoting free-space permeability, and ϵ_0 denoting free-space permittivity. $\boldsymbol{\rho}$ denotes observation position vector. $H_0^{(2)}(\cdot)$ is the Hankel function of the second kind of order zero, representing outgoing cylindrical waves in the wave propagation solution.

The formulation of the scattered field can be derived from the boundary condition [i.56]:

$$E_z^s = -\frac{\omega\mu_0}{4} I_t \sum_{n=-\infty}^{\infty} \Gamma_n H_n^{(2)}(k_0\rho_t) H_n^{(2)}(k_0\rho) e^{jn(\varphi-\varphi_t)} \tag{5.2-10}$$

with scattering coefficient:

$$\Gamma_n = -\frac{J_n(k_0 a)}{H_n^{(2)}(k_0 a)} \tag{5.2-11}$$

where $H_n^{(2)}(\cdot)\ and\ J_n(\cdot)$ are the Hankel function of the second kind and the Bessel function of the first kind respectively, with n being the order of the functions.

For electrically small cylinders $2a/\lambda_0 < 0{,}1$, where λ_0 denotes the wavelength of the incident electromagnetic wave in free space:

$$E_z^s \approx -\frac{\omega\mu_0}{4} I_t \left(-\frac{J_0(k_0 a)}{H_0^{(2)}(k_0 a)}\right) H_0^{(2)}(k_0\rho_t) H_0^{(2)}(k_0\rho) \tag{5.2-12}$$

After analysing the scattering from a single cylindrical element, the scattering problem of two small cylinders is then examined. In this case each cylinder acts as a scattering point, and their mutual electromagnetic coupling should be considered. The two cylinders may represent two scattering points of the same or different targets.

Consider two small PEC cylinders with radii a and b, located at positions $\boldsymbol{\rho}_1$ and $\boldsymbol{\rho}_2$ respectively as shown in Figure 5.2-5 (a). Each cylinder generates equivalent secondary currents: I_1^S and I_2^S. By considering that the scattered field from one cylinder serves as an additional incident field on the other, the corresponding equivalent currents should satisfy the following relationship:

$$I_1^S = \Gamma_0(k_0 a)\left[H_0^{(2)}(k_0\rho_{1t}) I_t + H_0^{(2)}(k_0\rho_{12}) I_2^S\right] \tag{5.2-13}$$

$$I_2^S = \Gamma_0(k_0 b)\left[H_0^{(2)}(k_0\rho_{2t}) I_t + H_0^{(2)}(k_0\rho_{12}) I_1^S\right] \tag{5.2-14}$$

where $\Gamma_0(\cdot) = -J_0(\cdot)/H_0^{(2)}(\cdot)$. The distance between two entities e_1 and e_2 is defined as:

$$\rho_{e_1 e_2} = \|\boldsymbol{\rho}_{e_1} - \boldsymbol{\rho}_{e_2}\|.$$

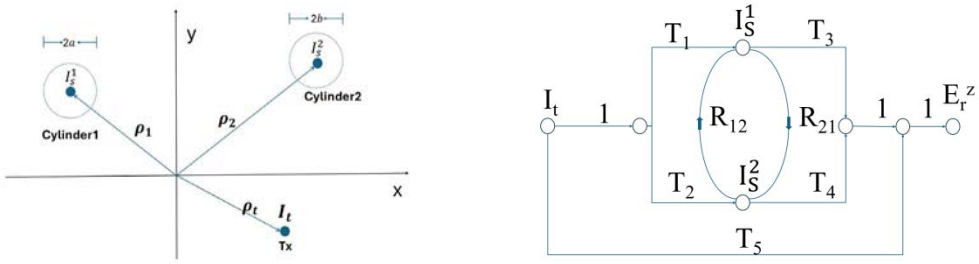

(a) (b)

Figure 5.2-5: Schematic and Signal flow diagram of two coupled cylinders with a radiation source

According to equations (5.2-13) and (5.2-14), the total received field can be represented using a signal flow graph, as illustrated in Figure 5.2-5 (b). The formula is obtained through the derivation based on the signal flow graph:

$$E_z^r = I_t\left(T_5 + \frac{T_1T_3+T_2T_4+T_1R_{12}T_4+T_2R_{21}T_3}{1-R_{12}R_{21}}\right) \quad (5.2\text{-}15)$$

where $T_5 = -\frac{\omega\mu_0}{4}H_0^{(2)}(k_0\rho_{rt})$ represents the direct propagation from the line source to the receiver. $T_1 = \Gamma_0(k_0a)H_0^{(2)}(k_0\rho_{1t})$ and $T_2 = \Gamma_0(k_0a)H_0^{(2)}(k_0\rho_{2t})$ denote the path gains due to propagation and cylinder scattering from the line source to Cylinder 1 and Cylinder 2, respectively. $T_3 = -\frac{\omega\mu_0}{4}H_0^{(2)}(k_0\rho_{r1})$ and $T_4 = -\frac{\omega\mu_0}{4}H_0^{(2)}(k_0\rho_{r2})$ denote propagation response from Cylinder 1 and Cylinder 2 to the receiver. $R_{12} = \Gamma_0(k_0a)H_0^{(2)}(k_0\rho_{12})$ and $R_{21} = \Gamma_0(k_0b)H_0^{(2)}(k_0\rho_{12})$ denote the mutual scattering response between two cylinders.

Unlike the proposed EM method, the segmentation method neglects electromagnetic coupling effects between targets. To quantitatively assess this difference, this clause computes the far-field RCS for two small cylinders using both approaches. This comparison directly illustrates the impact of inter-target coupling on scattering characteristics and highlights the limitations of the segmentation method.

Based on RCS definition, the complete monostatic RCS expression based on EM method becomes:

$$\sigma_{\mathrm{EM}} = \frac{4}{k_0}\cdot\frac{\left|\Gamma_a+\Gamma_b e^{-2jk_0d\cos\theta}+2\Gamma_a\Gamma_bH_{12}e^{-jk_0d\cos\theta}\right|^2}{\left|1-\Gamma_a\Gamma_bH_{12}^2\right|^2} \quad (5.2\text{-}16)$$

with

$$H_{12} = H_0^{(2)}(k_0d)$$

where d denotes the centre-to-centre separation distance between two small cylinders. θ is defined as the angle between the incident wave vector and the vector connecting the centres of the two cylinders.

The RCS calculated using the segmentation method can be expressed as:

$$\sigma_{\mathrm{seg}} = \frac{4}{k_0}\left||\Gamma_a| + |\Gamma_b|e^{-2jk_0d\cos\theta}\right|^2 \quad (5.2\text{-}17)$$

where $\Gamma_a = \Gamma_0(k_0a)\ and\ \Gamma_b = \Gamma_0(k_0b)$. Considering the mutual coupling is negligible ($H_{12}\rightarrow 0$), the following equation is achieved:

$$\sigma_{\mathrm{EM}} \rightarrow \sigma_{\mathrm{seg}} \quad (5.2\text{-}18)$$

Next, the discrepancy in 2D RCS calculations between the proposed EM-based method and the conventional segmentation approach is examined. Simulations are conducted for operations in both the 28 GHz and 15 GHz frequency bands, corresponding to wavelengths of λ_0 = 10,7 mm and λ_0 = 20 mm, respectively. For sensing target modelling, two cylinders with identical radii of 0,428 mm are considered. To further investigate the impact of the inter-cylinder distance d on the RCS, the incidence angle θ is fixed at 45°, and the RCS variation is analysed as a function of d. The inter-cylinder distance represents either the separation between two distinct targets or the spacing between two scattering points belonging to the same target.

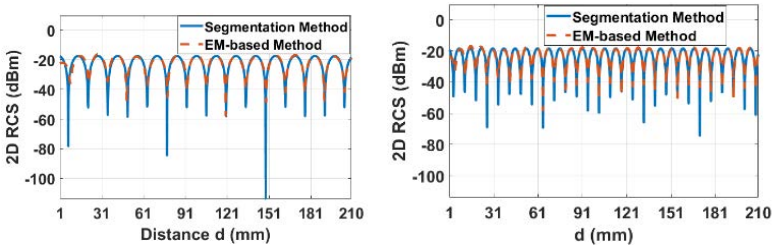

(a) 15 GHz (b) 28 GHz

Figure 5.2-6: Variation of 2D RCS with respect to d at 28 GHz and 15 GHz

Figure 5.2-6 highlights a key flaw in conventional non-coupled methods: by ignoring mutual coupling, they can deviate by over 20 dB from the discrete scattering model as d varies, showing that interactions cause strong interference in the total scattered field.

Since incident angle also affects RCS, the discrepancy between segmentation and EM-based models is quantified over multiple angles using the RMSE:

$$RMSE(d) = \sqrt{\frac{1}{M}\sum_{m=1}^{M}\left[\sigma_{\text{seg}}(\theta_m, d) - \sigma_{\text{EM}}(\theta_m, d)\right]^2} \tag{5.2-19}$$

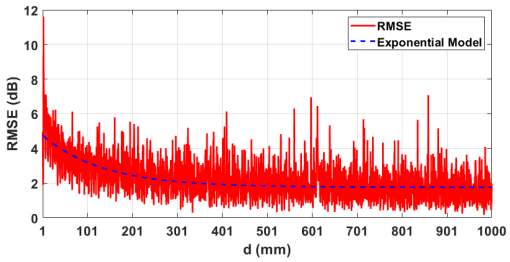

Figure 5.2-7: Variation of RMSE with respect to d

Figure 5.2-7 illustrates the variation of RMSE with separation distance d, where the decreasing RMSE with increasing d indicates a gradual weakening of mutual coupling effects. This trend can be derived from equation (5.2-16): the inter-cylinder coupling is described by Hankel functions $H_0^{(2)}(kd)$, whose magnitudes decay asymptotically as $|H_0^{(2)}(kd)| \sim \sqrt{2/(\pi kd)}$ for large kd. Accordingly, the coupling strength diminishes as d increases, in line with the observed RMSE reduction. Moreover, an exponential fitting model represented by the dashed curve in Figure 5.2-7 quantitatively captures this behaviour, confirming that the coupling-induced deviation decays exponentially with distance d, albeit with a specific offset (1,76 dB) that becomes observable at larger separation distances between scattering points.

$$RMSE(d) = 3{,}02e^{-\frac{d}{100}} + 1{,}76 + F_{\text{deviation}} \tag{5.2-20}$$

Equation (5.2-20) is the fitting result, where d is expressed in millimetres， and $F_{\text{deviation}}$ denotes the deviation of the actual RMSE from the fitted mean. As Figure 5.2-8 shows, $F_{\text{deviation}}$ can be modelled as a variable that follows a Gaussian distribution.

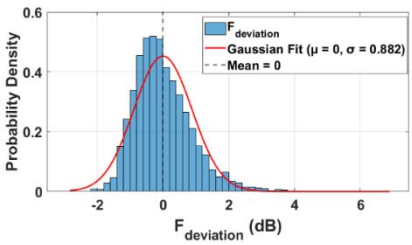

Figure 5.2-8: Distribution of $F_{\text{deviation}}$

Our EM-based model inherently captures spatial correlation by letting mutual coupling decay with scatterer separation. In contrast, the exponential autocorrelation function adopted in [i.2] for spatial consistency treats both small- and large-scale parameters as samples from a spatially correlated random field. These parameters vary smoothly with position, ensuring that the correlation between any two locations $\boldsymbol{r}_1$ and $\boldsymbol{r}_2$ follows an exponential model:

$$\mathrm{Corr}\big(X(\boldsymbol{r}_1), X(\boldsymbol{r}_2)\big) = e^{-\frac{\|\boldsymbol{r}_1-\boldsymbol{r}_2\|}{d_{\mathrm{corr}}}} \tag{5.2-21}$$

where d_{corr} is the autocorrelation distance of channel parameter.

To compare the approach, normalization is performed and the correlation distance used in both models is set to the same value $d_{\mathrm{corr}} = 100\ mm$ for fitting.

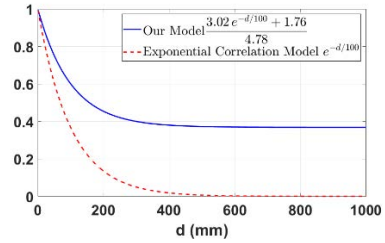

Figure 5.2-9: Comparison between two Models

Our model shows that the correlation caused by coupling effect between the two remains nonzero at any distance manifesting, for example, as a residual term in the fit unlike conventional exponential correlation model, which approaches zero.

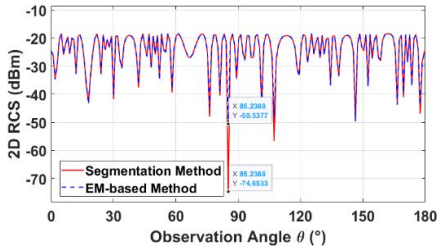

Figure 5.2-10: RCS varies with observation angles when d = 1 000 mm

That is because: when d is large, both denominator $1 - \Gamma_a \Gamma_b H_{12}^2 \to 1$ and $2\,\Gamma_a \Gamma_b H_{12} e^{-jk_0 d\cos\theta} \to 0$. However, at distances and angles satisfying $e^{-2jk_0 d\cos\theta} = -1$, the segmentation method's interference term cancels completely, whereas the coupling model retains a nonzero mutual-coupling contribution. For instance, at d = 1 000 mm and certain observation angles (Figure 5.2-10), the coupling model predicts significantly higher RCS than the decoupled approach. This residual term thus yields a nonzero RMSE.

Different coverage ranges affect target separation, so two 2D scenarios are evaluated—indoor office (12 m radius) and Urban Microcell (UMi, 115 m radius). In each, a π/3-rad sector is defined and two cylinders are uniformly placed at random. BS locations are excluded in the joint near-field (Rayleigh criterion) and 10 000 trials to histogram are run.

From Figure 5.2-11, it can be observed that the UMi scenario exhibits a lower mean of $\Delta\sigma$ compared to the indoor office scenario. This indicates that the segmentation approach generally shows better agreement with the EM method in the UMi scenario. The standard deviation of $\Delta\sigma$ reaches 1,82 dB in indoor office scenarios, which is significantly higher than the 1,35 dB observed in UMi environments, reflecting a wider distribution attributed to the closer proximity of targets and the resulting stronger mutual coupling effects in indoor environments.

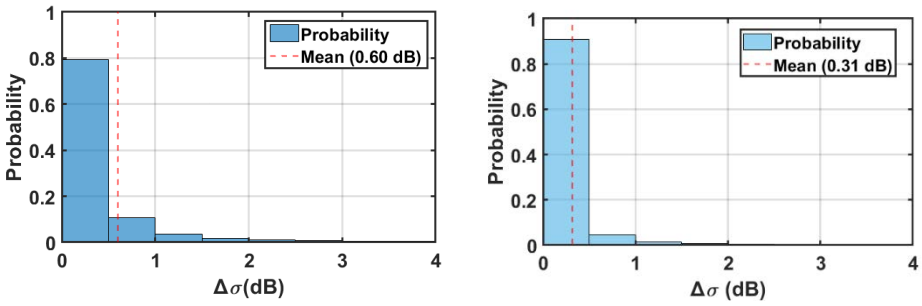

(a) Indoor Office (b) UMi

Figure 5.2-11: Distribution of $\Delta\sigma = |\sigma_{\mathrm{seg}} - \sigma_{\mathrm{EM}}|$ for two scenarios

From the numerical results, it is evident that the proposed methods provide significant improvements in modelling accuracy by accounting for coupling effects between scattering points. Notably, the method is derived rigorously from first principles, starting from Maxwell's equations, to analytically address the scattering behaviours of multiple regular scatterers (e.g. small cylindrical components). This physics-based approach ensures that the solution is grounded in electromagnetic theory rather than empirical fitting.

5.3 Micro-Doppler Modelling

5.3.1 Micro-Doppler definition

In ISAC channel, the micro-Doppler effect is defined as the change in the frequency or the phase of the reflected signal from the sensing target, wherein this change is induced by the target fine motion (e.g. rotation, vibration, hand gestures, etc.) [i.26] and [i.27]. Target fine motion generates sideband shifts about the target main Doppler frequency shift (e.g. that results from the bulk motion of the target). Compared to Doppler frequency shift, micro-Doppler frequency shift introduces time-variant function on the frequency or the phase of the reflected signal from the target.

5.3.2 Micro-Doppler Dependencies

The micro-Doppler effect is dependent on several factors:

1) Target fine motion amplitude: The amplitude may be dependent on the fine motion displacement as in the vibration motion or target geometry as in the case of the propeller rotation motion, where the micro-Doppler effect generated is dependent on the propeller size.

2) Target fine motion frequency: Target fine motion can be composed of single frequency component or multiple frequency components, where each frequency component may have different amplitude.

3) Target fine motion periodicity: The fine motion of the target may be classified into periodic (rotation, vibration, human walking, etc.) and aperiodic fine motion (e.g. human hand gestures, human standing-up/sitting-down, etc.).

4) Carrier frequency of the incident radio signal: The ratio between the fine-motion amplitude and the carrier wavelength impacts the micro-Doppler signature of the target fine motion. For example, the maximum micro-Doppler frequency shift amplitude increases as the wavelength of the incident radio signal decreases.

5) Target fine motion direction: The micro-Doppler effect is dependent on the angle between the incident radio signal and the target fine motion direction.

5.3.3 Proposed Modelling

Suppose that there are one point-scatter, which is moving as combination of several basic motions such as translation, vibration, rotation, coning, swinging, tumbling and others [i.3], [i.4], [i.5]. Doppler frequency shift induced by the point scatter's motion is obtained:

$$f_D = \frac{2}{\lambda}\left[\tilde{\boldsymbol{v}}_{\text{macro}} + \frac{d}{dt}(\tilde{\boldsymbol{p}}_t)\right]^T \tilde{\boldsymbol{r}}(t)$$

$$= \frac{2}{\lambda}\tilde{\boldsymbol{v}}_{\text{macro}}^T\tilde{\boldsymbol{r}}(t) + \frac{2}{\lambda}\tilde{\boldsymbol{v}}_{\text{micro}}^T(t)\tilde{\boldsymbol{r}}(t)$$

$$= \frac{2}{\lambda}\tilde{\boldsymbol{v}}_{\text{macro}}^T\tilde{\boldsymbol{r}}(t) + f_{\text{micro}}(t) \quad (5.3\text{-}1)$$

where $\lambda$is wavelength of carrier frequency. $\tilde{\boldsymbol{v}}_{\text{macro}}$is a vector representing the macro translation velocity. $\tilde{\boldsymbol{r}}(t)$ is the unit radial vector between point scatter and sensing device (suppose a mono-static sensing mode, bi-static mode will be considered in following part). The terms related to micro-Doppler are consisted of $\tilde{\boldsymbol{p}}_t$, $\tilde{\boldsymbol{v}}_{micro}(t)$ and $f_{micro}(t)$:

- $\tilde{\boldsymbol{p}}_t$ is the vector of micro-motion displacement;
- $\tilde{\boldsymbol{v}}_{micro}(t) = \frac{d\tilde{\boldsymbol{p}}_t}{dt}$is the vector of instantaneous velocity of micro-motion;
- $f_{micro}(t) = \frac{2}{\lambda}\tilde{\boldsymbol{v}}_{micro}^T(t)\tilde{\boldsymbol{r}}(t) = \frac{2}{\lambda}\frac{d\tilde{\boldsymbol{p}}_t^T}{dt}\tilde{\boldsymbol{r}}(t)$ is scalar value of instantaneous micro-Doppler frequency.

Thus, for one point scatter, the phase due to the Doppler frequency shift for micro-motion can be described as following:

$$exp\left(j2\pi\frac{2\int\tilde{\boldsymbol{r}}(t)^T\tilde{\boldsymbol{v}}_{\text{micro}}(t)dt}{\lambda}\right) \quad (5.3\text{-}2)$$

In summary, The micro-Doppler frequency should be modelled per ray, and each ray can be seen from one single point scatter.

For the case of far field and the direct path between sensing transceiver and the sensing target, the Doppler phase formula for m-th ray in n-th cluster in a link of Tx-ST-Rx in a time t can be given by:

$$exp\left(j2\pi\frac{\int_0^t\tilde{\boldsymbol{r}}_{\text{rx},n,m}^T(\tau)\tilde{\boldsymbol{v}}_{\boldsymbol{rx}}d\tau}{\lambda_0}\right)exp\left(j2\pi\frac{\int_0^t\tilde{\boldsymbol{r}}_{\text{tx},n,m}^T(\tau)\tilde{\boldsymbol{v}}_{\boldsymbol{tx}}d\tau}{\lambda_0}\right)$$

$$exp\left(-j2\pi\frac{\int_0^t\tilde{\boldsymbol{r}}_{\text{rx},n,m}^T(\tau)\tilde{\boldsymbol{v}}_{\text{macro},n,m}d\tau}{\lambda_0}\right)exp\left(-j2\pi\frac{\int_0^t\tilde{\boldsymbol{r}}_{\text{tx},n,m}^T(\tau)\tilde{\boldsymbol{v}}_{\text{macro},n,m}d\tau}{\lambda_0}\right)$$

$$exp\left(-j2\pi\frac{\int_0^t\tilde{\boldsymbol{r}}_{\text{rx},n,m}^T(\tau)\tilde{\boldsymbol{v}}_{\text{micro},n,m}(\tau)d\tau}{\lambda_0}\right)exp\left(-j2\pi\frac{\int_0^t\tilde{\boldsymbol{r}}_{\text{tx},n,m}^T(\tau)\tilde{\boldsymbol{v}}_{\text{micro},n,m}(\tau)d\tau}{\lambda_0}\right) \quad (5.3\text{-}3)$$

in which $\tilde{\boldsymbol{r}}_{tx,n,m}$ is the unit radial vector from sensing transmitter to sensing scatter point target of m-th ray in n-th cluster, and $\tilde{\boldsymbol{r}}_{rx,n,m}$ is the unit radial vector from sensing receiver to sensing scatter point target of m-th ray in n-th cluster. $\tilde{\boldsymbol{v}}_{\text{macro},n,m}$is the velocity of macro-motion of sensing scatter point target related to m-th ray in n-th cluster and $\tilde{\boldsymbol{v}}_{\text{micro},n,m}(\tau)$ is the instantaneous velocity of micro-motion of sensing scatter point target related to m-th ray in n-th cluster at time of τ:

- If the simulation assume that duration time is short compared to the moving speed of targets, Tx and Rx, in which the geometry relationship of targets, Tx and Rx do not change significantly, the $\tilde{\boldsymbol{r}}_{\text{rx,n,m}}(\tau)$ and $\tilde{\boldsymbol{r}}_{\text{tx},n,m}(\tau)$ are approximated as $\tilde{\boldsymbol{r}}_{\text{rx,n,m}}$and $\tilde{\boldsymbol{r}}_{\text{tx,n,m}}$as ETSI TR 138 901 [i.2]. The Doppler phase formula can be simplified as:

$$exp\left(j2\pi\frac{\tilde{\boldsymbol{r}}_{\text{rx},n,m}^T\left[\tilde{\boldsymbol{v}}_{\text{rx}}t-\left(\tilde{\boldsymbol{v}}_{\text{macro},n,m}t+\tilde{\boldsymbol{\varphi}}_{\text{micro},n,m}(t)\right)\right]}{\lambda_0}\right)exp\left(j2\pi\frac{\tilde{\boldsymbol{r}}_{\text{tx},n,m}^T\left[\tilde{\boldsymbol{v}}_{\text{tx}}t-\left(\tilde{\boldsymbol{v}}_{\text{macro},n,m}t+\tilde{\boldsymbol{\varphi}}_{\text{micro},n,m}(t)\right)\right]}{\lambda_0}\right) \quad (5.3\text{-}4)$$

with $\tilde{\boldsymbol{\varphi}}_{\text{micro},n,m}(t) = \int_0^t\tilde{\boldsymbol{v}}_{\text{micro},n,m}(\tau)d\tau = \int_0^t\frac{d}{d\tau}(\tilde{\boldsymbol{p}}_{\tau,n,m})d\tau = \tilde{\boldsymbol{p}}_{t,n,m} - \tilde{\boldsymbol{p}}_{0,n,m}$ is the integration of velocity of micro-motion, which is also vector of micro-motion displacement.

In [i.3], [i.4] and [i.6], the functions of different motions/gestures are researched, and some models have been provided based on numerous measurements and simulations. Those outcomes can serve as the starting point. The following formulas are proposed for further study.

The following micro-motion formula can be studied as the starting point.

Table 5.3-1: Micro-Doppler functions for motions

Type of target	Type of motion	Formula of micro-Doppler function $\bar{\varphi}_{micro}(t)$
Single scatter point	Vibration [i.3]	$\overline{\varphi}_{micro}(t) = R_0 + \bar{\boldsymbol{r}}_v D_v \sin\omega_v t$ $\bar{\boldsymbol{r}}_v$ is the unit radial vector of vibration direction D_v is the amplitude of vibration $\omega_v = \frac{2\pi}{f_v}$ and f_v is the frequency of vibration
Single scatter point	Rotation [i.3]	$\bar{\boldsymbol{\varphi}}_{micro}(t) = \boldsymbol{R}_t \cdot \boldsymbol{R}_{init} \cdot \bar{\boldsymbol{r}}_p$ $\boldsymbol{R}_t = I + \hat{\boldsymbol{\omega}}' \sin\Omega t + \hat{\boldsymbol{\omega}}'^2(1 - \cos\Omega t)$ is the rotation matrix at times t $\boldsymbol{R}_{init}$ is the initial rotation matrix $\bar{\boldsymbol{r}}_p$ is location vector of scatter point
Helicopter rotor blades	Rotation [i.6]	$\bar{\boldsymbol{\varphi}}_{micro,k,p}(t) = R + \bar{\boldsymbol{r}}_h l(p) \cos(\Omega t + \phi_0 + \frac{k2\pi}{N})\ \left(k = 0,1,\cdots,N-1\,; p = 1,\cdots,N_p\right)$ For $p$thscatter point on the $k$thblade $R$is the initial location offset and $\phi_0$is the initial phase $\bar{\boldsymbol{r}}_h$ is the location vector of helicopter $l(p)$ is the length between $p$thscatter point and centre of blades $\Omega = \frac{2\pi}{f}$ and $f$is the frequency of blade rotation
UAV blades	Rotation [i.6]	$\bar{\boldsymbol{\varphi}}_{micro,k,p}(t) = R_j + \bar{\boldsymbol{r}}_u L_2 \cos\left(\Omega_j t + \phi_j + \frac{k2\pi}{N_B}\right)\ (j = 1,\cdots,N_R\,; k = 0,\cdots,N_B - 1)$ For kth rotation blade on the jth rotor of UAV $R_j$is the initial location offset of jth rotor and $\phi_j$is the initial phase of jth rotor $\bar{\boldsymbol{r}}_u$is the location vector of UAV $L_2$is the distance between the centre of blade and the centre of the rotation $\Omega_j = \frac{2\pi}{f_j}$ and $f_j$is the frequency of jth blade rotation
Human	Respiration [i.6]	$\bar{\boldsymbol{\varphi}}_{micro}(t) = R_0 + \bar{\boldsymbol{r}}_p D_{max} \sin(2\pi f_r t)$ $R_0$is the initial location offset $\bar{\boldsymbol{r}}_p$is the location vector of human D_{max} is the maximum amplitude of respiration $f_r$is the frequency of respiration
Human	Heartbeat [i.6]	$\bar{\boldsymbol{\varphi}}_{micro}(t) = R_0 + \bar{\boldsymbol{r}}_p D_{max} \sin(2\pi f_r t)$ $R_0$is the initial location offset $\bar{\boldsymbol{r}}_p$is the location vector of human D_{max} is the maximum amplitude of heartbeat $f_r$is the frequency of heartbeat
Human	Walking or running [i.6]	$\bar{\boldsymbol{\varphi}}_{micro}(t) = R_0 + \bar{\boldsymbol{r}}_p \sum_{p=1}^{N_p} D_p \sin\left(2\pi f_p t\right)$ $R_0$is the initial location offset $\bar{\boldsymbol{r}}_p$is the location vector of human $N_p$is the number of human segments $D_p$is the maximum amplitude of motion of pth segment f_p is the frequency of motion of pth segment

5.3.4 Evaluation methodology and feasibility analysis

5.3.4.1 Simulation on link-level system

A simulation for sensing of micro-motion is carried on link-level system. CDL-B channel model defined in ETSI TR 138 901 [i.2] is used, in which the 16th cluster is seen as sensing cluster related to sensing target with speed of 150 km/h at x axis of GCS and other clusters are thought as environmental cluster with zero speed. Besides, the cluster-wise rms azimuth spread of arrival angles (cluster ASA), cluster-wise rms azimuth spread of departure angles (cluster ASD), cluster-wise rms zenith spread of arrival angles (cluster ZSA), and cluster-wise rms zenith spread of departure angles (cluster ZSD) of 16th cluster are all set to 2°, which is much smaller than the defined value in ETSI TR 138 901 [i.2] because only sensing LoS channel (only reflected and scattered by sensing target) is used for simulation currently and it is expected that one sensing point should not correspond to that large angle spread. The other sensing signal and channel configuration is list in Table 5.3-2.

Table 5.3-2: Sensing signal and channel configuration

Carrier frequency f	3,5 GHz
Sub carrier space Δf	30 kHz
Bandwidth of sensing signal B	18 MHz
Number of rays in one cluster	20
Pulse repetition interval of sensing signal	14 OFDM symbol
Time length of sensing signal	1 OFDM symbol
Sensing signal repetition number	50
Spread of angles in sensing cluster	**2°**
Port number of receiver antenna	16
SNR	30 dB
Speed of sensing target	150 km/h

Table 5.3-3: CDL-B channel in ETSI TR 138 901 [i.2]

Cluster #	Normalized delay	Power in [dB]	AoD in [°]	AoA in [°]	ZoD in [°]	ZoA in [°]
1	0,0000	0	9,3	-173,3	105,8	78,9
2	0,1072	-2,2	9,3	-173,3	105,8	78,9
3	0,2155	-4	9,3	-173,3	105,8	78,9
4	0,2095	-3,2	-34,1	125,5	115,3	63,3
5	0,2870	-9,8	-65,4	-88,0	119,3	59,9
6	0,2986	-1,2	-11,4	155,1	103,2	67,5
7	0,3752	-3,4	-11,4	155,1	103,2	67,5
8	0,5055	-5,2	-11,4	155,1	103,2	67,5
9	0,3681	-7,6	-67,2	-89,8	118,2	82,6
10	0,3697	-3	52,5	132,1	102,0	66,3
11	0,5700	-8,9	-72	-83,6	100,4	61,6
12	0,5283	-9	74,3	95,3	98,3	58,0
13	1,1021	-4,8	-52,2	103,7	103,4	78,2
14	1,2756	-5,7	-50,5	-87,8	102,5	82,0
15	1,5474	-7,5	61,4	-92,5	101,4	62,4
16	**1,7842**	**-1,9**	**30,6**	**-139,1**	**103,0**	**78,0**
17	2,0169	-7,6	-72,5	-90,6	100,0	60,9
18	2,8294	-12,2	-90,6	58,6	115,2	82,9
19	3,0219	-9,8	-77,6	-79,0	100,5	60,8
20	3,6187	-11,4	-82,6	65,8	119,6	57,3
21	4,1067	-14,9	-103,6	52,7	118,7	59,9
22	4,2790	-9,2	75,6	88,7	117,8	60,1
23	4,7834	-11,3	-77,6	-60,4	115,7	62,3

Per-Cluster Parameters					
Parameter	cASD in [°]	cASA in [°]	cZSD in [°]	cZSA in [°]	XPR in [dB]
Value	10	22	3	7	8

Besides the speed of translation motion equal to 150 km/h which is macro-motion, random part of rays in sensing cluster is added same micro-Doppler phase based on the given micro-Doppler function. Two different micro-Doppler functions are used as follows.

Table 5.3-4: Micro-Doppler mode used

Parameters	Mode 1	Mode 2
Number of rays adding micro-Doppler	6	8
Maximum speed of micro-Motion (m/s)	50	30
Micro-Doppler function	$f_{micro}(t) = 50\,cos\left(\frac{2\pi\Delta f}{3}t\right)$	$f_{micro}(t) = 30\text{sawtooth}\left(\frac{2\pi\Delta f}{5}t\right)$

5.3.4.2 Sensing parameters estimation

Firstly, the estimated CSI from received echo signal has three dimensions, spatial-frequency-slow time. An incoherent merge is done at the dimension of the spatial, because the precise angle of arrival of potential target in each frequency-slow time sampling window is unknown. The merged result only has two dimensions: frequency-slow time, which can be transferred into delay-Doppler domain, showing as Figure 5.3-1.

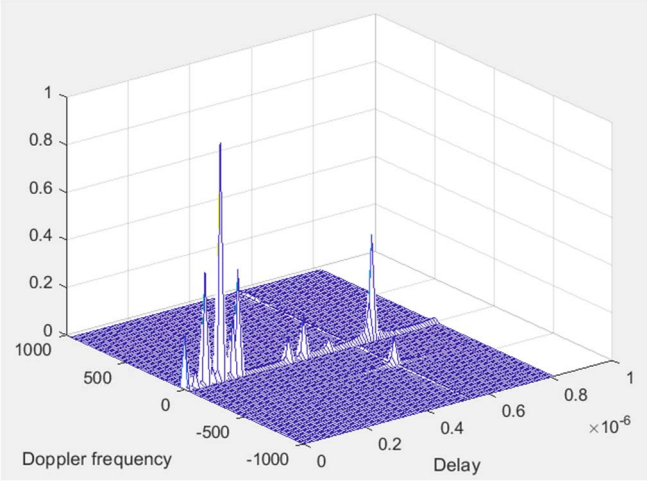

Figure 5.3-1: Delay-Doppler profile of channel merged in spatial domain

It can be seen environmental channel has a high power around zero Doppler frequency, which can be eliminate by zero notch filter. Difference operation is done along the dimension of slow time for each slice of slow time value, environmental channel with zero Doppler value can be suppressed and sensing channel with large Doppler value will not be effected. The Delay-Doppler profile after difference operation is shown in Figure 5.3-2.

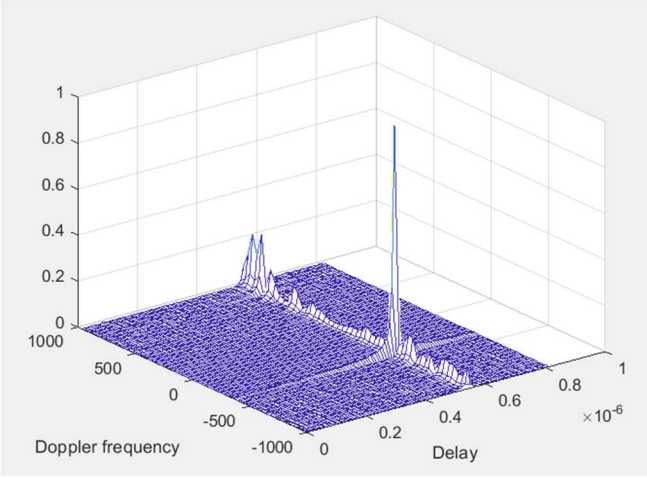

Figure 5.3-2: Delay-Doppler profile of channel after difference

The maximum peak in Figure 5.3-2 is the peak of sensing target, which can be used to estimate the delay and velocity of sensing target. The delay error of simulation result is 21 ns and Doppler error is 0,61 Hz, which are all smaller than resolution. Therefore, the estimation can be used for micro-Doppler classification. Select all Doppler value along axis of Doppler of the found peak of sensing target, and all these Doppler values are used as input features for micro-Doppler pattern classification.

5.3.4.3 Classification of micro-Doppler mode

Firstly, the Doppler values of two micro-Doppler modes are checked without any noise. It can be seen that different micro-Doppler modes have different Doppler patterns, and the difference of them can be used for classification.

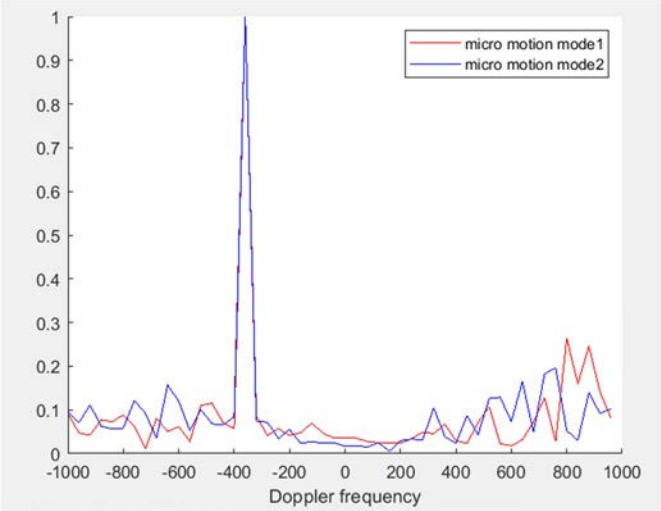

Figure 5.3-3: Doppler pattern of two micro-Doppler mode

Under a SNR of 30 dB, a sequence of Doppler vector data (comprising 50 PRIs) detected in the delay-Doppler profile for sensing a target was selected as the input to perform a binary classification aimed at distinguishing whether the micro-Doppler signatures belong to mode 1 or mode 2. Initially, Principal Component Analysis (PCA) was conducted on the Doppler vector data of length 50 to assess the compressibility of the 100-dimensional Doppler vector data (treating the real and imaginary parts separately). The results reveal that the explained variance percentages (interpreted as weights) across different dimensions of the micro-Doppler data are relatively dispersed, indicating that collecting data across more Doppler dimensions is crucial for micro-Doppler classification.

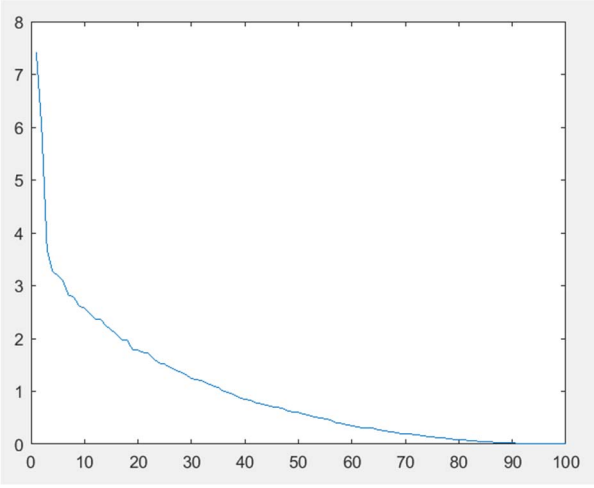

Figure 5.3-4: Weights of PCA results

Binary classification is considered as a relatively simple classification task. Support Vector Machine (SVM) is employed to learn from the dataset and carry out the classification task. Each of the two micro-motion modes generates 100 sets of micro-Doppler channel data, totalling 200 sets of data, utilizing ten-fold cross-validation (90 % of data for training and 10 % for testing).

At a Signal to Noise Ratio (SNR) of 30 dB, the classification plane formed by the support vectors and the visualization of the classification results are as follows: It is evident that at an SNR of 30 dB, the Doppler features caused by different micro-motion models have significant differences, allowing for clear separation.

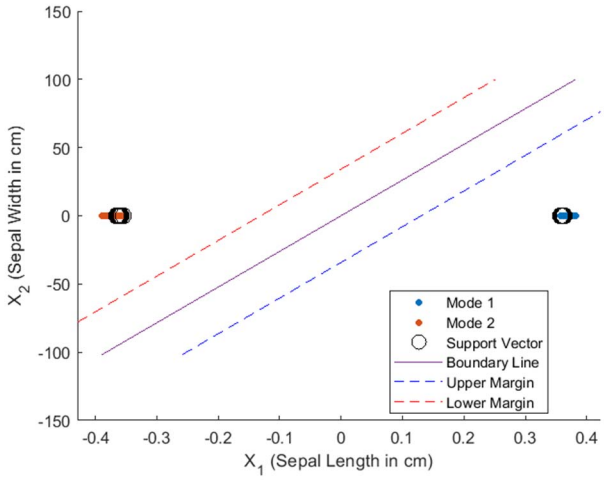

Figure 5.3-5: The classification plane at an SNR of 30 dB

At a SNR of 0 dB, the classification plane formed by the support vectors visualizes as shown in Figure 5.3-6.

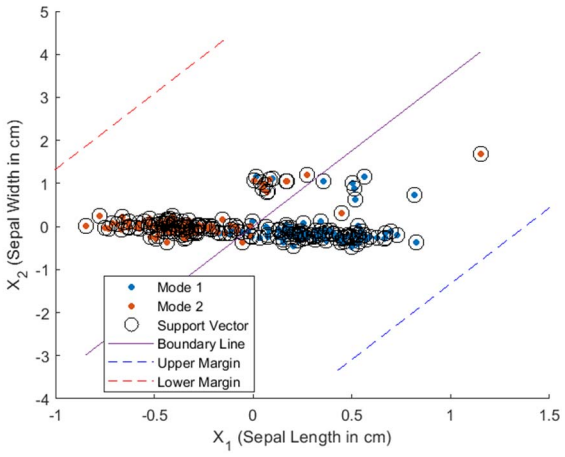

Figure 5.3-6: The classification plane at an SNR of 0 dB

The error rates in valid dataset with the change of SNR are shown in Table 5.3-5.

Table 5.3-5: Error rates in different SNR conditions

SNR	Error rates in valid dataset
30	0
20	0
10	0
0	0,065
-10	0,45
-20	0,45
-30	0,42

5.4 Micro-deformation channel modelling

5.4.1 Definition

Micro-deformation sensing stands as a cornerstone in the realm of structural health monitoring for buildings, bridges, and mining-sites. This technology plays a pivotal role in offering insights into the structural integrity of infrastructure, unveiling hidden deformation patterns arising from daily activities, and serving as an early warning system by detecting abnormal patterns.

5.4.2 Proposed methodology for modelling

To evaluate the feasibility of the micro-deformation detection based on wireless-sensing method, e.g. based on the base station sensing, accurate channel modelling is extremely essential.

The CloudRT simulator [i.36] describes the propagation process and provides detailed information of the Multipath Components (MPCs), accounting for Line of Sight (LoS), reflection, scattering, diffraction, and transmission. RT simulation works under various scenarios including outdoors and indoors. In addition, both static scenario like living room and dynamic scenario like high-speed railway can be simulated by RT simulator, whose adaptable working frequencies are from a few hundred MHz to around 300 GHz. Accurate RT simulation results [i.37] allow for the detailed modelling of real-world environments such as buildings, bridges, and terrain, etc. In contrast, stochastic geometry models use probabilistic distributions to describe the environment and often overlook the specific impact of objects. Therefore, RT-based method is appropriate for detecting the micro change of objects in a relatively big area.

In this proposal, an RT-based method is proposed to detect the oscillation of the bridge floor. RT is used for important information obtaining and deformation levels' judging.

The following procedures in Figure 5.4-1 can be considered.

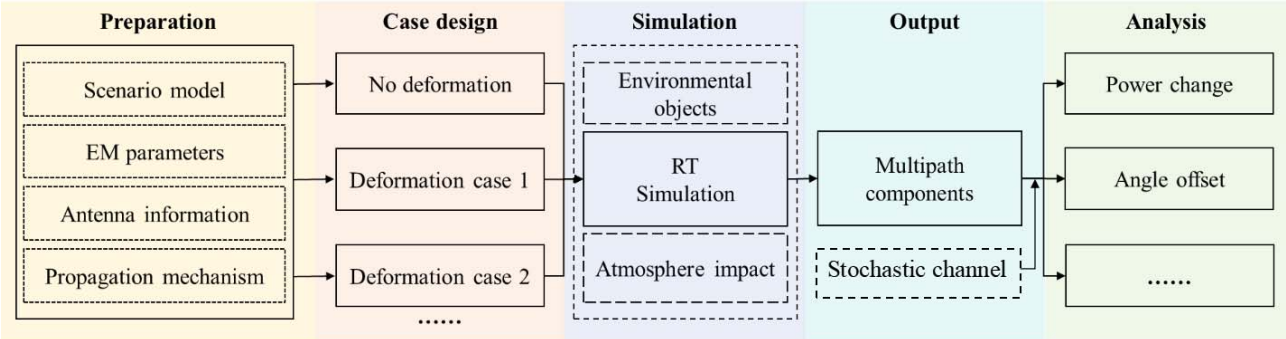

Figure 5.4-1: RT-based micro-deformation detection methodology

Step 1: preparing the models, parameters and making case design for the RT simulation.

Firstly, the overall bridge scenario is modelled, and a metal surface with a side length of 25 cm is designed to make the deformation more detectable. The RT simulation scenario for micro-deformation is shown in Figure 5.4-2 and Figure 5.4-3. The height of the bridge floor is 19,7 m. The Base Station (BS) is located 106 m from the front end of the bridge floor, with three metal surfaces placed on the side closer to the BS, separating by 61,6 m, respectively. The area within the blue dashed line represents the region where micro-deformations are considered, which is 261,1 m long and 37,2 m wide.

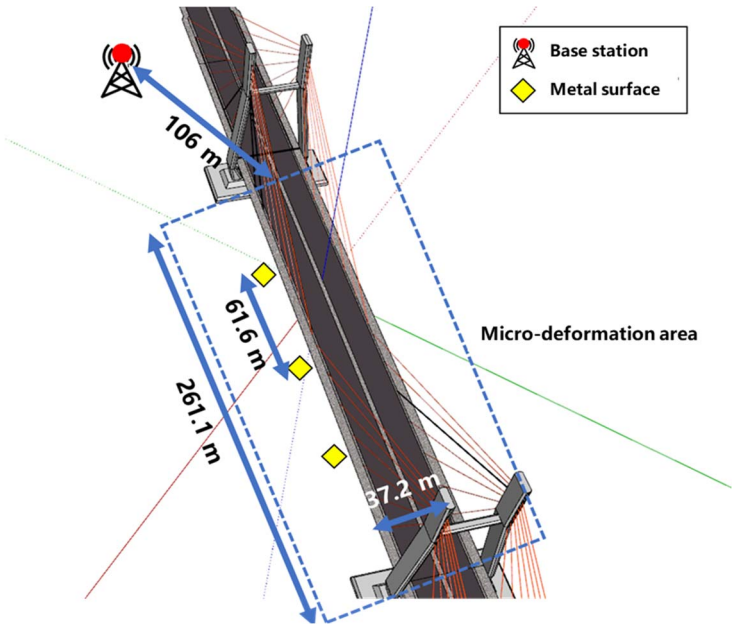

Figure 5.4-2: Simulation scenario

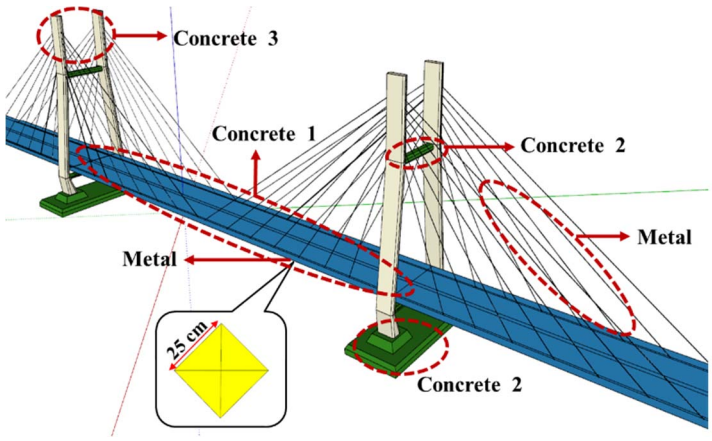

Figure 5.4-3: Modelling of bridge scenario

As shown in Figure 5.4-4 and Figure 5.4-5, different vibration levels of the bridge floor are modelled.

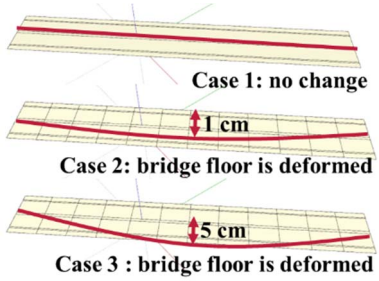

Figure 5.4-4: Cases of different vibration levels of bridge floor

Initially, three cases with "no change" and "1 cm micro-deformation" and "5 cm micro-deformation" are considered. It is marked in Figure 5.4-5 that three metal surfaces are set in the 1/4, 1/2, and 3/4 place of one side of the bridge, respectively.

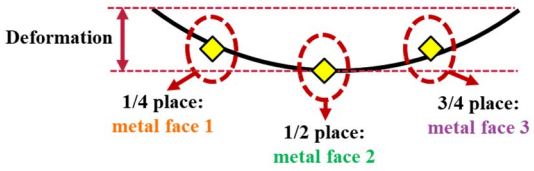

Figure 5.4-5: Positions of metal surfaces of the bridge

Step 2: adding environmental objects such as vehicles, pedestrians if necessary.

The presence of environmental objects, such as vehicles and pedestrians, can be considered into the RT simulations for micro-deformation detection in bridge scenarios. Therefore, the integration of these elements into the simulation environment is planned. By adding vehicles and pedestrians, a more realistic representation of actual traffic conditions can be achieved. Figure 5.4-6 gives the case that there are cars on the bridge floor.

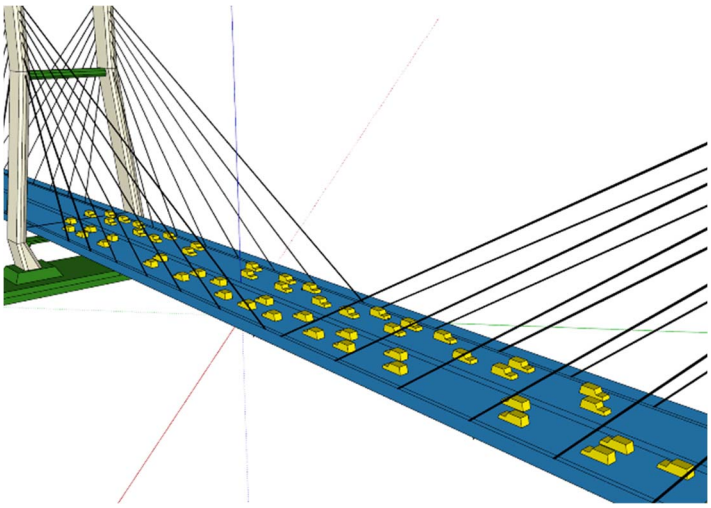

Figure 5.4-6: Bridge scenario with cars

This enhancement will facilitate the observation of how these environmental factors influence the propagation of electromagnetic waves and the resulting MPCs information. Specifically, the focus will be on analysing the effects on angles of arrival, received power, and other critical parameters that contribute to assessing the bridge's oscillation. Understanding these interactions will be crucial for determining the impact of vehicles and pedestrians on the detection of the bridge micro-deformation.

Step 3: adding geometry-based stochastical channel model for background surroundings if necessary.

RT-simulation scheme faces problem of generalization because wireless channel derived by 3D model used in RT is fixed. The channel model for evaluation micro-deformation could consider adding geometry-based stochastic channel defined in ETSI TR 138 901 [i.2] as background surroundings. The stochastic channel would be generated as clusters and rays according to scenario configuration, including UMi, UMa, RMa, Indoor and so on:

$$H_{sim} = H_{RT} + H_{38,901} \quad (5.4\text{-}0)$$

EXAMPLE: One bridge is assumed to be deployed at RMa scenario. The background channel could be added by including stochastic channel with configuration of RMa, making the channel model for simulation mimic random real-work conditions with higher generalizability. Figure 5.4-7 gives the case that there are surroundings around the bridge, in which the background channel is given by generated stochastical channel.

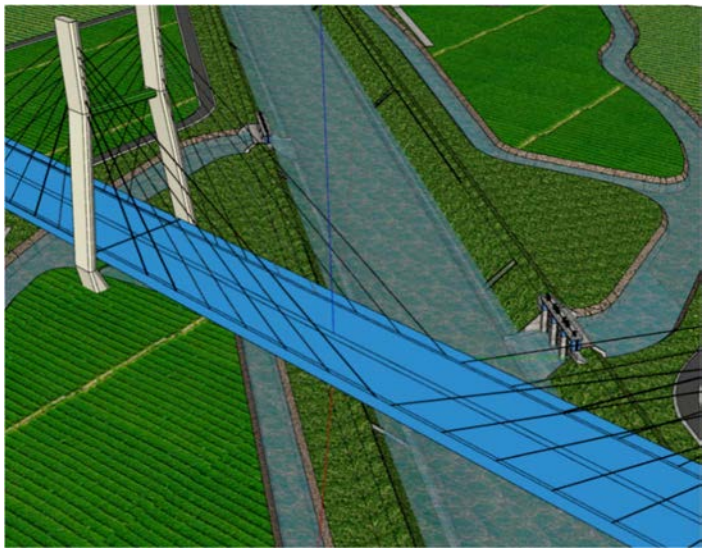

Figure 5.4-7: Bridge scenario with surroundings

Step 4: adding atmosphere impact if necessary.

The inclusion of atmospheric effects, such as various weather conditions, can be considered if necessary for RT simulations aimed at micro-deformation detection in real bridge scenarios. Whether or not these atmospheric variables should be integrated depends on the frequency band used and the specific environment. In cases where higher-frequency bands are involved, conditions like heavy rainfall, dense fog, snowfall, or humidity fluctuations may have a significant impact on radio propagation and need to be factored into the RT simulation. Figure 5.4-8 shows possible environmental conditions that can be considered in the scenario.

Figure 5.4-8: Bridge scenario under different environmental conditions

By selectively incorporating these weather conditions when relevant, the simulations can provide a more accurate reflection of real-world communications. However, for lower-frequency bands where atmospheric effects are less prominent, it might not be essential to account for these factors. This approach ensures that atmospheric impacts are considered only when they are likely to influence the results.

By including atmospheric factors, the method can be optimized for different frequency bands and environmental scenarios, ultimately contributing to more accurate and reliable detection.

Step 5: initialize EM parameters of materials.

Electromagnetic (EM) parameters are given for various materials in the scenario. The materials for the bridge model are set as three types of concrete, while the suspension cables are modelled using metal. The detailed information of EM parameters is shown in Table 5.4-1.

Table 5.4-1: The EM parameters in simulation

Object	Material	Real part of relative permittivity	Loss tangent	Directive scattering coefficient	Equivalent roughness
Bridge floor	Concrete 1	1,44	0,075	0,33	2
Pier	Concrete 2	1,00	0,100	0,76	1
Pillar	Concrete 3	1,92	0,030	0,17	5
Metal surfacer	Metal	1,00	10^7	0,85	15

Step 6: initialize propagation mechanism.

The principle of the used propagation mechanism in simulation is shown in Table 5.4-2.

Table 5.4-2: The propagation mechanism and the principle in simulation

Propagation mechanism	Geometric calculation	Electromagnetic calculation
Reflection	Snell's Law [i.38]	Fresnel equation
Scattering	Directive scattering [i.39]	Scattering coefficient and equivalent roughness

Step 7: obtaining the MPCs from the deterministic RT simulation.

Based on the model information, antenna specifications, material EM parameters, and other necessary simulation configurations, the RT simulation can be conducted to obtain multipath information. By modelling the bridge under different deformation scenarios and performing RT simulations, MPCs under various conditions are gathered. The data provides insights into the energy levels and angles of arrival for each path, which are critical for understanding how structural changes influence propagation.

Then the data is analysed to obtain the energy, angles, and other characteristics, allowing for the computation and extraction of relevant channel parameters. By comparing these parameters, the degree of deformation in the bridge can be accessed, and the accuracy and precision of the proposed RT method for micro-deformation detection can be validated. For instance, a notable increase in delay spread or angular spectrum explains that the structural integrity of the bridge has been compromised.

5.4.3 Evaluation methodology and feasibility analysis

5.4.3.1 Simulation assumption

In the following simulation, the simulation frequency is 4,9 GHz, with a bandwidth of 100 MHz and 4 096 sampling points. The BS is at a height of 30 m, utilizing the omni-directional antenna both for transmitting and receiving. The detailed simulation configuration and the antenna pattern can be seen in Table 5.4-3 and Figure 5.4-9.

The impact of weather on signal propagation is highly dependent on the frequency band. In higher frequency bands, such as millimeter-wave and terahertz frequencies, atmospheric conditions, including rain, fog, and humidity, significantly affect signal attenuation and performance. However, in the case of the bridge scenario under consideration, where the operating frequency is 4,9 GHz, a relatively lower frequency, the influence of weather is minimal. Given the reduced sensitivity of lower frequencies to atmospheric conditions, it is unnecessary to incorporate weather effects into the simulation for this particular scenario at low frequency band.

In addition, because of the high altitude of BS and bridge, LoS condition is assumed between BSs and the metal surfaces of the bridge. For simplicity, no vehicles/pedestrians are assumed on the bridge in this simulation.

Table 5.4-3: Simulation configuration

Parameter	Value
Frequency [GHz]	4,9
Bandwidth [MHz]	100
Sampling points	4 096
BS location [m]	(-77,64, -173,53)
Antenna height [m]	30
Antenna type	omni-directional
Transmitting power [dBm]	43
Propagation mechanism	1st reflection, 1st scattering
Metal surface side length [cm]	25
Simulation case	Case 1, Case 2, Case 3

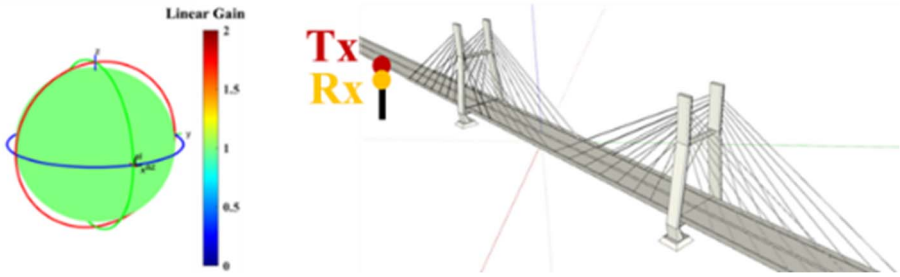

Figure 5.4-9: The antenna pattern and deployment

5.4.3.2 Feasibility analysis based on simulation results

Based on the 3D model, the material parameters, the frequency, the propagation mechanism, and the antenna information, extensive RT simulations are carried out. According to the description in the four steps above, the MPCs information are calculated. Figure 5.4-10 shows the MPCs in one case of the bridge scenario.

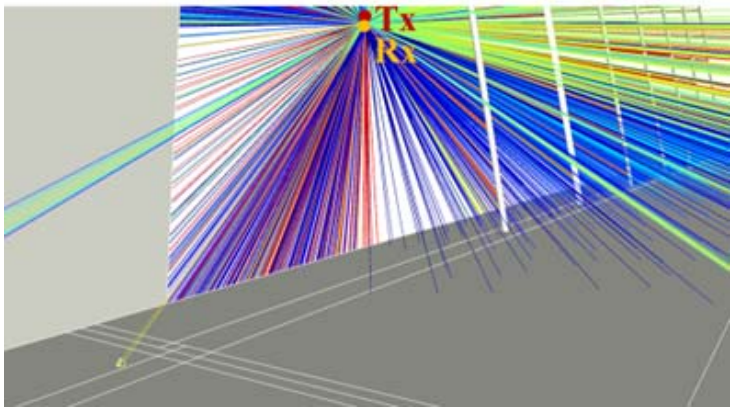

Figure 5.4-10: The MPCs in the bridge scenario

A single simulation case can be completed in seconds, and the results between different deformation levels are provided here. Through the calculation of RT simulation, the power delay profiles of three cases are shown in Figure 5.4-11.

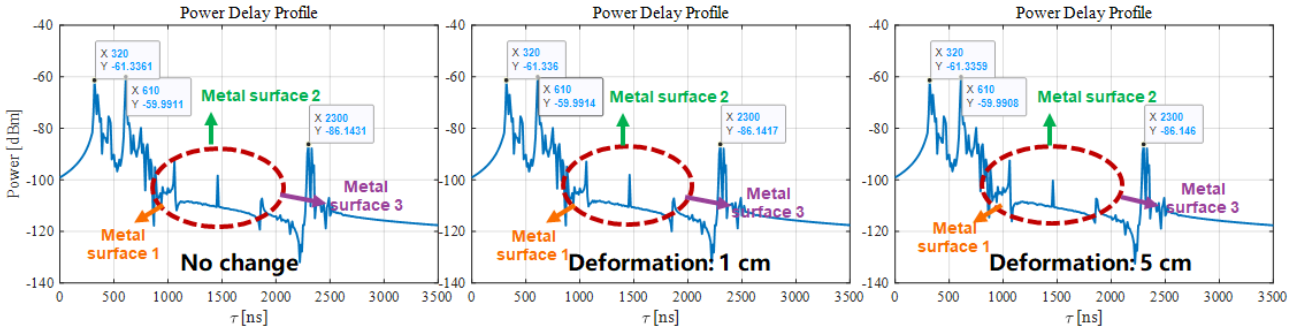

Figure 5.4-11: Power delay profiles of three cases

The time delays corresponding to the maximum power are marked, which are caused by the reflection of the relatively dense and complex structure of the bridge's suspension cable. In each case, the power of -61,34 dBm corresponding to the of the delay of 320 ns, the power of -59,99 dBm corresponding to the of the delay of 610 ns, the power of -86,14 dBm corresponding to the of the delay of 2 300 ns. Since only the bridge floor vibrates rather than other structures, the change of these are not obvious. Because the material of the bridge is concrete, it is difficult to observe the influence of its micro-deformation, so the effect of observing the metal surface on one side of the bridge is better.

To observe the influence of the micro-deformation of the bridge floor, only the angular energy spectrum of the metal surface is analysed since only the bridge and the metal on it oscillates in the scenario. The angular energy spectrums of three deformation levels' cases are obtained and compared in Figure 5.4-12.

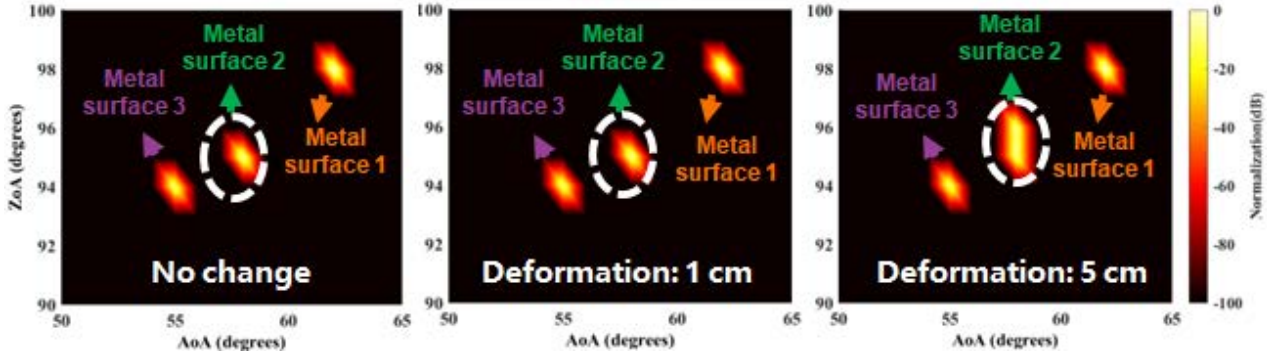

Figure 5.4-12: Angular energy spectrums of three cases

The corresponding phase change of three metal surfaces with three cases are obvious when the bridge deforms. It can be verified that when the bridge floor sinks 5 cm, the arrival angle of the 4,9 GHz echo changes significantly.

Through further analysis of RT simulation results, specific MPCs phase changes caused by micro-deformation can be obtained, and the detailed calculation is shown in Figure 5.4-13. Firstly, 1st scattering and 1st reflection are selected in this RT simulation since the transmitter antenna and the receiver antenna are placed together. After RT simulation, MPCs are obtained and delay profile for each frequency are calculated. Through Fast Fourier Transform (FFT), complex Channel Transfer Function (CTF) can be acquired. Then after calculating the phase angle of it, the phase change caused by micro-deformation can be detected.

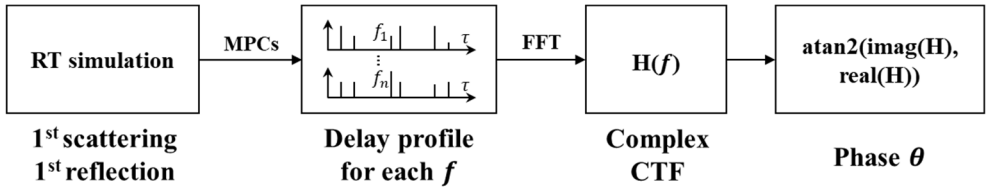

Figure 5.4-13: Calculation of the phase change caused by micro-deformation

The comparison of three metal surfaces in case 1 "no change", case 2 "1 cm deformation", case 3 "5 cm deformation" is shown in Figure 5.4-14. Phase of three metal surfaces in different cases can be obtained through the detection. As the bridge floor vibrates up and down in three cases, the phase of metal surface 1 changes from -103,42° to -111,07° and further to -141,68° from case 1 to case 2 to case 3, the phase of metal surface 2 changes from 94,54° to 83,40° and further to 38,80° from case 1 to case 2 to case 3, and the phase of metal surface 3 changes from 8,14° to 3,78° to -13,69° from case 1 to case 2 to case 3. Therefore, through RT simulations, the change process of phase can be observed when the bridge floor oscillates. That is to say, it is feasible that the change of the deformation can be accurately, efficiently and low-cost detected based on the phase detection.

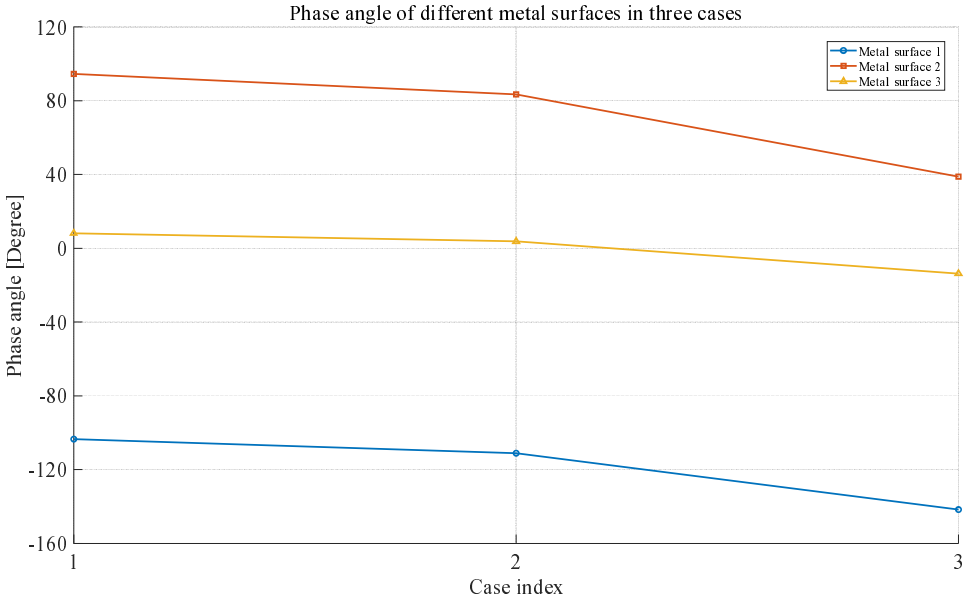

Figure 5.4-14: Angle and power comparison of three cases

From the phase change with different amount of deformation, noted as $\Delta deformation$, the mapping from phases to amount of micro-deformation can be calculated using:

$$\Delta deformation = \frac{\Delta phase}{2\pi} \times \lambda, \quad (5.4\text{-}1)$$

where the $\Delta phase$ in radians represents the phase change between amount of micro-deformation, λ is the wavelength in metre and $\lambda = c/f$, where c is 3×10^8 m/s and f is the carrier frequency in Hz. Based on equation (5.4-1), $\Delta deformation$ observed by base station can be obtained. Details of phases to amount of micro-deformation mapping are presented in Table 5.4-4.

Table 5.4-4: Mapping from phases to amount of micro-deformation

Metal surface	Case design	$\Delta phase$ [°]	$\Delta deformation$ [cm]
Metal surface 1	1 cm deformation (Case 1 to Case 2)	7,65	0,130
	4 cm deformation (Case 2 to Case 3)	30,61	0,521
	5 cm deformation (Case 1 to Case 3)	38,26	0,651
Metal surface 2	1 cm deformation (Case 1 to Case 2)	11,14	0,189
	4 cm deformation (Case 2 to Case 3)	44,60	0,759
	5 cm deformation (Case 1 to Case 3)	55,74	0,948
Metal surface 3	1 cm deformation (Case 1 to Case 2)	4,36	0,074
	4 cm deformation (Case 2 to Case 3)	17,47	0,297
	5 cm deformation (Case 1 to Case 3)	21,83	0,371

From Table 5.4-4, it can be observed that the phase changes obtained through multipath generated by RT simulation can quantify the bridge micro-deformation. The calculated amount of bridge deformation is less than the actual amount in real case design due to the long distance between the BS and the observation point of the bridge (i.e. metal surfaces along the side of the bridge), and the angle of the incident signal from BS to the observation point of the bridge. The amount of deformation of different metal surfaces has different proportions with phase angle, since when the bridge vibrates the central place (metal surface 2) of the bridge has the biggest deformation, while the other two are at 1/4 places of the bridge with smaller numerical changes. Therefore, the mapping formula for the deformation can be modified as follows:

$$\Delta deformation' = modified\ factor\ \times \frac{\Delta phase}{2\pi} \times \lambda, \quad (5.4\text{-}2)$$

where the $modified\ factor$ is related to the position of BS related to the observation point of the bridge. Specifically, when the metal surfaces are placed at different points of the side of the bridge while the height of the BS is determined, various distances make the elevation angle between the observation point and the BS differ. The spatial angle and the distance affect the factor by determining the position of the BS, that is, the relative relationship between BS and the observation point on the metal surface. Since the direction of the micro-deformation is certain in this bridge scenario (bridge just vibrates up and down in the vertical plane), the $modified\ factor$ can be described by the elevation angle between the observation point and the BS as follows:

$$modified\ factor = \frac{1}{2*\sin(\theta)}, \quad (5.4\text{-}3)$$

where θ is the elevation angle of the path between the metal surface and the BS. Based on the phase angle change from the RT results, the amount of the deformation can be calculated accurately given that the factor in the simple scenario with the direction of the deformation are known. For the bridge floor from the 1/4 place (where metal surface 1 setting) to 3/4 place (where metal surface 3 setting), the changes of the factor reflect the relation between the phase angle change and the amount of the bridge micro-deformation.

According to the formula of the factor and the data of metal surface 2, the $modified\ factor$=5,2 is considered as the factor in this simulation scenario, which can be used to describe the deformation in case design, and the result is presented in Table 5.4-5. By adding this new factor, this new deformation is same to that of real movement. By doing this, the deformation is accurately detected through the phase angle calculated from RT simulation results within 2 % of the deformation displacement.

Table 5.4-5: $\Delta deformation$ with $modified\ factor$

Metal surface	Case design [cm]	$\Delta deformation$ [cm]	$\Delta deformation$ with $modified\ factor$ [cm]	Error [cm]
Metal surface 2	1	0,189	0,983	0,0170 (1,70 %)
	4	0,759	3,947	0,0530 (1,33 %)
	5	0,948	4,930	0,0700 (1,40 %)

For the metal surface 1 and metal surface 2, the model of the $modified\ factor$ also are verified to be effective. Due to the different elevation angle between the observation point and the BS, the factor varies. Additionally, because of the positions the metal surfaces are placed, the 1/4 and 3/4 places are with smaller numerical changes, which is about 1/2 of that in the case design. The $modified\ factor$ for these two metal surfaces are validated in Table 5.4-6.

Table 5.4-6: $Modified\ factor$ validation for surface 1 and surface 3

Metal surface	Case design [cm]	$modified\ factor$ [cm]	$\Delta deformation$ with $modified\ factor$ [cm]	Error [cm]
Metal surface 1	1 (0,5)	3,80	0,494	0,0060 (1,20 %)
	4 (2)		1,980	0,0200 (1,00 %)
	5 (2,5)		2,474	0,0260 (1,04 %)
Metal surface 3	1 (0,5)	6,65	0,492	0,0080 (1,60 %)
	4 (2)		1,975	0,0250 (1,25 %)
	5 (2,5)		2,467	0,0330 (1,32 %)

The simulation results demonstrate the efficiency of the RT method for detecting micro-deformations, as it successfully captures phase changes and the changes can be mapped to the deformation of the bridge. Additionally, this method shows potential for applications in a range of other detection scenarios, including natural disaster monitoring, etc. In summary, the RT approach for micro-deformation offers an advanced solution for precise and adaptable sensing, ensuring reliable performance in various detection tasks.

5.5 Rain Attenuation Modelling

5.5.1 Definition

In wireless communication systems, rain attenuation is defined as "the signal power loss caused by the absorption and scattering of electromagnetic waves by raindrops along the propagation path." A more comprehensive interpretation describes it as "the quantitative measure of the reduction in signal strength due to the interaction between transmitted radio waves and precipitation particles, expressed as a function of rainfall rate, frequency, polarization, and propagation path". Rain attenuation modelling characterizes the impact of meteorological conditions on signal integrity and is critical for designing reliable communication links [i.45], particularly in high-frequency bands (e.g. mmWave and THz). The modelling process requires accounting for factors such as spatial inhomogeneity of rainfall in short distances and scattering effects in high-frequency bands.

5.5.2 Rain Attenuation Model Dependencies

Rain attenuation represents the characteristic impairment caused by precipitation in wireless channels, Modelling the rain attenuation should take into consideration of the following parameters:

a) Frequency.

b) Rainfall Rate.

c) Polarization Mode.

d) Propagation Path Characteristics:

   i) Actual Path Length.

   ii) Elevation Angle.

   iii) Distance factor.

e) Compensation Factors:

   i) Short-Range Compensation.

   ii) High-Frequency Correction.

5.5.3 Rain Attenuation Model Application

6G, especially ISAC systems in dense urban environments require precise rain attenuation modelling to ensure stable mmWave signal transmission under heavy rainfall, while enabling dynamic optimization of short-range communication links. In dense vehicular networks, the model could enable real-time prediction of dynamic rain attenuation affecting V2V mmWave links. This capability would allow autonomous vehicles to dynamically coordinate perception and communication tasks using instantaneous channel quality feedback, ensuring stable environmental awareness and reliable data transmission even during heavy rainfall. For low-altitude drone operations essential to logistics and disaster response, the model might support intelligent mmWave link adaptation by analysing rain-induced signal distortions, potentially maintaining ultra-low-latency connectivity crucial for mission-critical operations.

Beyond ensuring communication reliability, the model could enable real-time environmental awareness through multi-source meteorological data fusion. By estimating rainfall rate from mmWave attenuation patterns, it facilitates dynamic reconstruction of urban rain environments, supporting applications like localized flood warnings and adaptive route planning.

5.5.4 Rain Attenuation Modelling Approaches

A fitting approach leveraging nonlinear least squares optimization is utilized to correct the parameter values of k and α by analyzing differential rain attenuation data derived from adjacent rainfall rate. These corrected parameters are then incorporated into the Recommendation ITU-R P.838-3 [i.42] model, along with attenuation values that include not only transmission loss but also the attenuation due to wet antenna effects across various frequencies. To enhance the model's accuracy, empirical compensation terms are introduced, considering both short-distance effects and high-frequency corrections. More specifically, the detailed establishment process of the proposed model is shown in Figure 5.5-1. This approach not only enhances the predictive capability for rain attenuation but also provides deeper insights into the physical mechanisms of rain-induced attenuation.

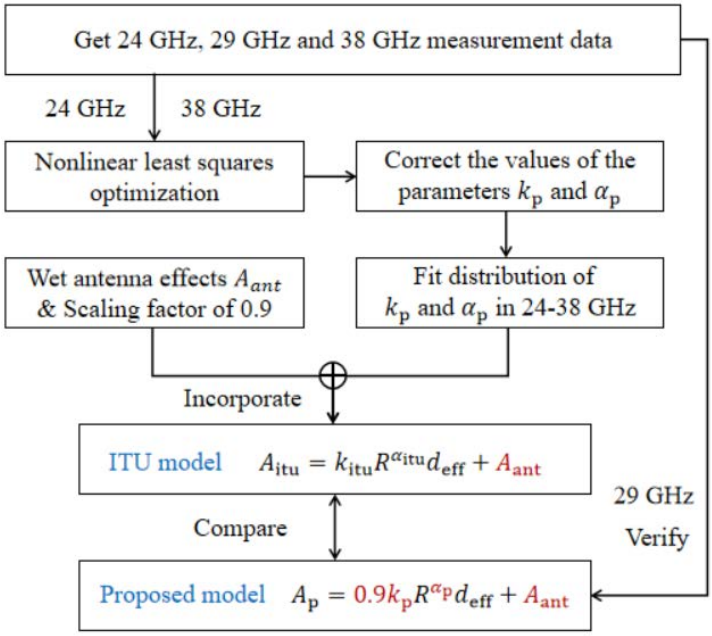

Figure 5.5-1: Flow chart of the establishment process of proposed model

A systematic calibration framework for the Recommendation ITU-R P.838-3 [i.42] rain attenuation model is developed through a combination of parameter optimization and empirical compensation. The methodology utilizes a constrained nonlinear least-squares algorithm to ascertain optimal coefficients by minimizing the residuals between modelled and measured differential attenuation. This process primarily involves using adjacent rainfall rate pairs and attenuation differences as inputs. Subsequently, the corrected parameters are incorporated into the standard ITU formulation via parameter substitution.

$$\gamma_p = k_p R^{\alpha_p}, \tag{5.5-1}$$

where γ_p is the optimized predicted attenuation, and k_p and α_p are the optimized parameters.

The detailed modelling steps are as follows:

Step 1 performs broad parameter exploration using multiple initial guesses:

- α near ITU baseline ±1 (physical constraint).
- Coarse convergence tolerance (0,1 % error allowed).

Step 2 conducts precise refinement with strict criteria:

- Ultra-fine tolerance (0,00001 % error).
- Maximum 2 000 iterations.

It not only avoids the defect of traditional single-stage optimization that is easy to fall into local optimum, but also maintains the interpretability of parameters through physical constraints, which provides a new methodological framework for millimeter wave rain attenuation modelling.

Based on actual physical limitations, two empirical adjustments are integrated to elevate the proposed model's predictive accuracy and practical applicability:

- **Short-path compensation:** Adds a scaling factor of 0,9 for links shorter than 1 km. This adjustment aims to improve the accuracy of the model when the rain rate varies sharply over short distances, taking into account the non-uniform distribution of rain over these short-range links [i.46].
- **High-frequency correction:** Reduces α by 0,05 for frequencies above 35 GHz. This adjustment accounts for the increased signal loss due to Mie scattering and other raindrop interactions at higher frequencies. This adjustment improves model accuracy for high-frequency applications [i.47].

5.5.5 Results Analysis

The optimized rain attenuation is obtained by integrating the corrected parameters into the ITU model formulation, and the corresponding wet antenna attenuation values are added to get the total rain attenuation. Furthermore, the errors between the results and the measurement are compared using the proposed model and ITU model, including the ME and RMSE. The result shows that the proposed model improves the fitting accuracy.

As shown in Figure 5.5-2, the proposed model at 24 GHz has resulted in improvements. As demonstrated in Table 5.5-1, Table 5.5-1 (a) presents the corrected k and α values at 24 GHz, while Table 5.5-1 (b) compares the measured attenuation under various rain rates with the predictions from the ITU model and the proposed model.

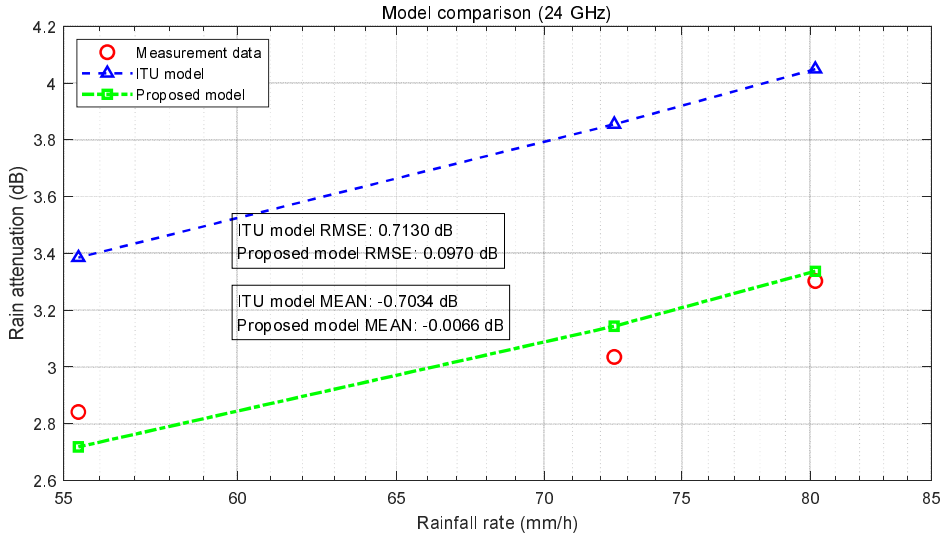

Figure 5.5-2: Comparison of rain attenuation prediction

Table 5.5-1: Optimization result of model at 24 GHz

(a) Summary of model parameters

Parameter	ITU model	Proposed model
k	0,1404	0,0014
α	0,9561	1,9561

(b) Comparison of modelling result of different models

Rainfall [mm/h]	Measurement[dB]	ITU model[dB]	Proposed model [dB]
80,2	3,3027	4,0492	3,3371
72,5	3,0347	3,8546	3,1434
55,4	2,8415	3,3851	2,7181

As shown in Figure 5.5-3, the proposed model at 38 GHz has resulted in significant improvements. As demonstrated in Table 5.5-2, Table 5.5-2 (a) presents the corrected k and α values at 38 GHz, while Table 5.5-2 (b) compares the measured attenuation under various rain rates with the predictions from the ITU model and the proposed model.

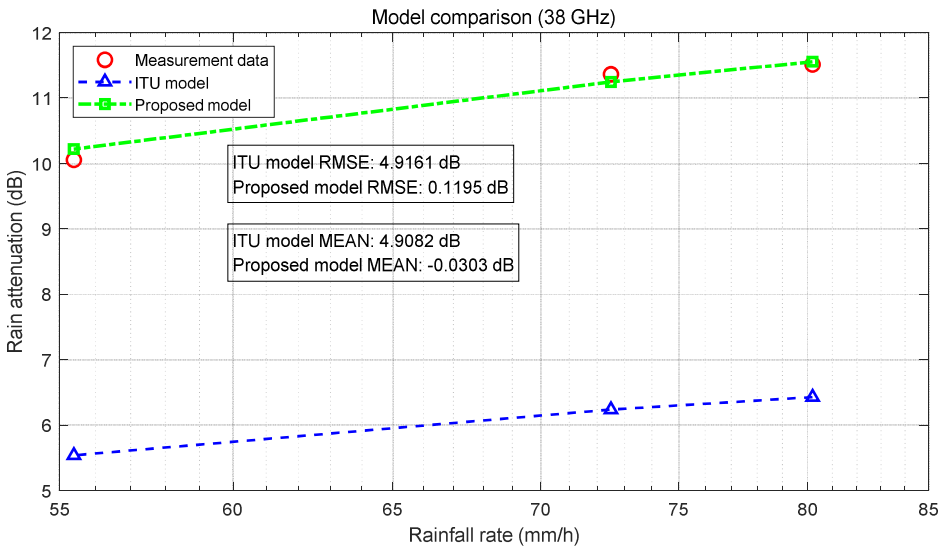

Figure 5.5-3: Comparison of rain attenuation prediction

Table 5.5-2: Optimization result of model at 38 GHz

(a) Summary of model parameters

Parameter	ITU model	Proposed model
k	0,3844	6,8791
α	0,8552	0,4500

(b) Comparison of modelling result of different models

Rainfall [mm/h]	Measurement[dB]	ITU model[dB]	Proposed model [dB]
80,2	11,5127	6,4287	11,5560
72,5	11,3635	6,2386	11,2462
55,4	10,0549	5,5391	10,2199

5.5.6 Model Verification

Continuous parametric distributions for 24 GHz to 38 GHz are established by fitting methods based on measured data points at 24 GHz and 38 GHz. Specifically, k values are fitted using an exponential function and α values through quadratic polynomial regression. This approach enables precise determination of both k and α coefficients at any frequencies within the 24 GHz to 38 GHz range, with complete distribution characteristics visualized in Figure 5.5-4. The specific parameter values for k and α are comprehensively tabulated in clause 5.5.7. In Figure 5.5-4, the fitted k and α parameter values are also compared against those provided in Recommendation ITU-R P.838-3 [i.42].

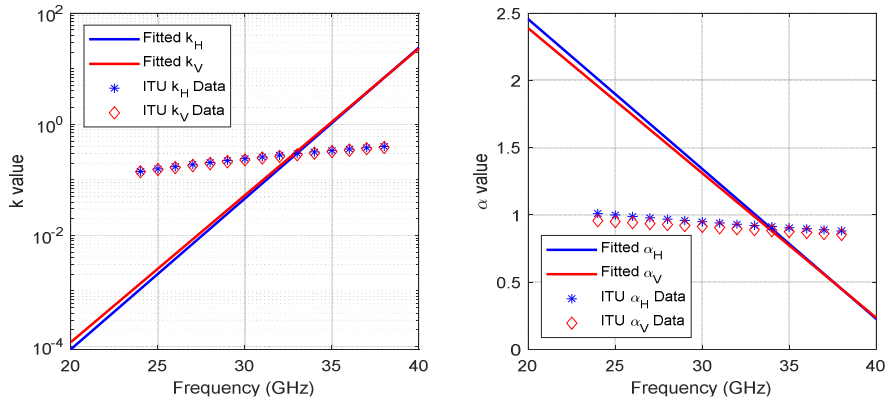

Figure 5.5-4: The distributions of the fitted k and α values

To validate the fitting results, two distinct rain rate conditions at 29 GHz are randomly selected for model validation, with detailed comparison results being presented in Table 5.5-3. This indicates that the proposed model is highly applicable to other frequencies within the millimeter wave frequency band.

Table 5.5-3: Model verification at 29 GHz

Rainfall [mm/h]	k (fitted)	α (fitted)	Measurement[dB]	Proposed model [dB]
72,5	0,0288	1,4182	4,5020	4,5711
62,8			4,2767	4,2149

Furthermore, the prediction accuracy of the ITU model and the proposed model is compared across three frequency bands, with performance quantified using ME and RMSE averaged over different rainfall rates. As shown in Table 5.5-4, the proposed model effectively enhances the predictive capabilities for rain attenuation.

Table 5.5-4: Comparison of model error

Frequency	ITU model		Proposed model	
	ME [dB]	RMSE [dB]	ME [dB]	RMSE [dB]
24 GHz	-0,7034	0,7130	-0,0066	0,0970
29 GHz	-0,2434	0,2460	-0,0037	0,0656
38 GHz	4,9082	4,9161	-0,0303	0,1195

It is expected to continue refining the rain attenuation model and expand measurement coverage to additional frequency bands, with specific emphasis on mmWave frequencies where raindrop size distribution critically affects signal attenuation due to shorter wavelengths and intensified scattering phenomena. Accordingly, focused investigations into raindrop size distribution can be conducted to quantify its impact on mmWave propagation.

Based on the above modelling approaches, analysis, and verification, the proposed modelling is as follows: for short-range links, the distance scaling factor is introduced to correct the effective path length d_{eff}, and the rain attenuation will be the sum of path attenuation and wet antenna attenuation, which is:

$$\mathrm{A_p} = \mathrm{k_p R^{\alpha_p} d_{eff}} \times 0{,}9 \; + \mathrm{A_{ant}} \tag{5.5-2}$$

For the proposed rain attenuation channel model, which is applicable in the mmWave band for short-range links (less than 1 km), the corrected k and alpha parameters are given by Table 5.5-5:

Table 5.5-5: Proposed model parameters

Frequency(GHz)	k_{pH}	α_{pH}	k_{pV}	α_{pV}
24	0,0011	2,0101	0,0014	1,9561
25	0,0020	1,8987	0,0025	1,8485
26	0,0038	1,7872	0,0046	1,7409
27	0,0071	1,6758	0,0085	1,6334
28	0,0132	1,5644	0,0157	1,5258
29	0,0248	1,4529	0,0288	1,4182
30	0,0463	1,3415	0,0529	1,3106
31	0,0865	1,2301	0,0972	1,2031
32	0,1616	1,1186	0,1787	1,0955
33	0,3019	1,0072	0,3284	0,9879
34	0,5642	0,8957	0,6034	0,8803
35	1,0542	0,7843	1,1087	0,7727
36	1,9700	0,6729	2,0373	0,6652
37	3,6812	0,5614	3,7437	0,5576
38	6,8790	0,4500	6,8791	0,4500

Total rain attenuation is measured, then subtract the path attenuation predicted by proposed model to get wet antenna effect attenuation, which is then fitted with an exponential distribution. Table 5.5-6 presents selected values from the example conditions studied.

Table 5.5-6: The measurement conditions

Rain rate(mm/h) / Frequency(GHz)	55,4	72,5	80,2
24	2,3423	2,5320	2,6032
29	2,8964	3,0861	3,1573
38	3,6878	3,8775	3,9487

The comparison results show the proposed model fits measurements in reality with high accuracy.

5.5.7 Proposed Model

Based on the measurement and fitting result mentioned in above contents, for short-range links, the distance scaling factor is introduced to correct the effective path length d_{eff}, and the rain attenuation will be the sum of path attenuation and wet antenna attenuation, which is:

$$A_p = 0{,}9\ k_p R^{\alpha_p} d_{eff} + A_{ant} \quad (5.5\text{-}3)$$

For the proposed rain attenuation channel model, which is applicable in the millimeter-wave band for short-range links (less than 1 km), the corrected k and alpha parameters are given by Table 5.5-5.

6 Conclusions and recommendations

The scope of the present document is to develop advanced ISAC channel models that fill certain gaps within existing channel models, and validate these through feasibility analysis. The present document is placed in the framework of other parallel initiatives ongoing worldwide and supported by the whole research ecosystem, including standardization bodies, industrial individual members and stakeholder associations, academia, strategic national and regional collaborative projects.

To set the foundations of ISAC, the present document gives an overview of the state-of-the-art ISAC channel modelling approaches including related academic literature, IEEE 202.11bf [i.1], ETSI TR 138 901 [i.2], and other forums. The limitations of these channel models are accordingly summarized.

Furthermore, the present document provides advanced modelling approaches including on RCS, micro-Doppler modelling, micro-deformation, and Rain attenuation modelling. Specifically:

- Segmentation approach is proposed which is a promising approach in building up an RCS model for complex objects using the pre-known RCS of basic objects. The resulting RCS model can be scalable to accommodate different frequency bands or object dimensions. Also, segmentation can be used to evaluate the RCS of electrically large sized objects at different separation distances from the Tx/Rx.

- Detailed micro-Doppler modelling is proposed through the real measurement campaigns and RT emulations. The suggested patterns can be used to for evaluation of the use cases of human motion recognition, the use case on real-time monitoring of health hazard and disaster risk, the use case on emergency search and rescue, the use case for healthcare sensing and monitoring, etc.

- Ray tracing based method is proposed to detect the micro-deformation of a bridge for the use case of structural health monitoring. The specific simulation scenario and procedures including parameters for different vibration levels of bridge floor, EM parameters of bridge materials, background modelling, etc. are provided.

- Rain attenuation modelling is proposed with adjustments of ITU-R recommendation for higher accuracy of rainfall monitoring. For short-range links, the distance scaling factor is newly introduced to correct the effective path length, and the rain attenuation is the sum of path attenuation and wet antenna attenuation. The adjusted parameter values are provided for millimetre-wave band.

In summary, it is recommended that the proposed ISAC channel models are considered in any further studies and specification work related to 6G ISAC systems, including ETSI ISG ISAC work streams on System and RAN Architectures [i.16] and on Security, Privacy, Trustworthiness and Sustainability for ISAC [i.17].

Annex A:
Measurement campaigns and emulations for micro-Doppler

A.1 Measurement campaign

As a way to minimize external clutters, an empty indoor environment was selected as the testing field for this investigation [i.4], see Figure A.1-1. As shown in Figure A.1-2, the room has a vertical dimension of 2,73 m and a total surface area of around 250 m^2.The radar is positioned at the centre of the space, oriented towards one of the walls. It is noticed that the wall placed opposite the radar is adorned with wallpaper composed of a distinct material compared to normal walls.

Figure A.1-1: Testing field in a vacant room

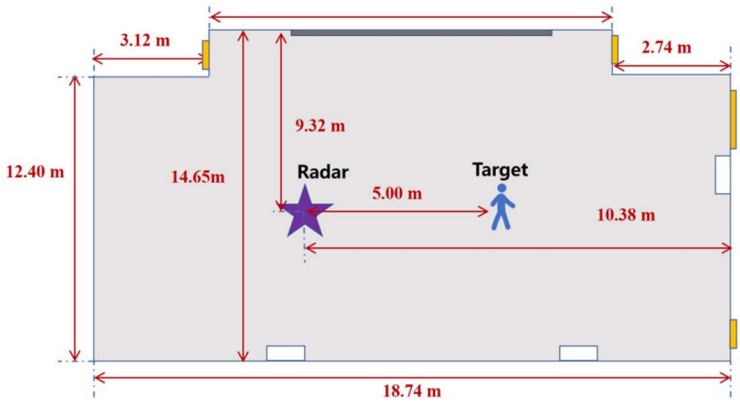

Figure A.1-2: Dimensions of the room and radar position

As shown in Figure A.1-3, the present investigation uses a millimetre wave radar board (red chip) in conjunction with the real-time Data Acquisition Card (DAC). Following pre-calculation, the linear velocity of the pedestrian's swinging arm is around 2 m/s. Consequently, the radar settings demonstrated in Table A.1-1 are modified to increase velocity resolution and achieve more accurate observations at this maximum detectable velocity.

Table A.1-1: Radar parameters

Parameter	Value
Speed of light [m/s]	3e8
Start frequency [GHz]	77
Available bandwidth [MHz]	1 605,72
Carrier frequency [GHz]	78,129
Maximum detection distance [m]	11,20
Range resolution [m]	0,093
Maximum detection speed [m/s]	2,40
Speed resolution [m/s]	0,069
Number of TX	2
Number of RX	4
Chirp loop per frame	70
Sample per chirp	120
Sampling rate [Mbps]	3,289

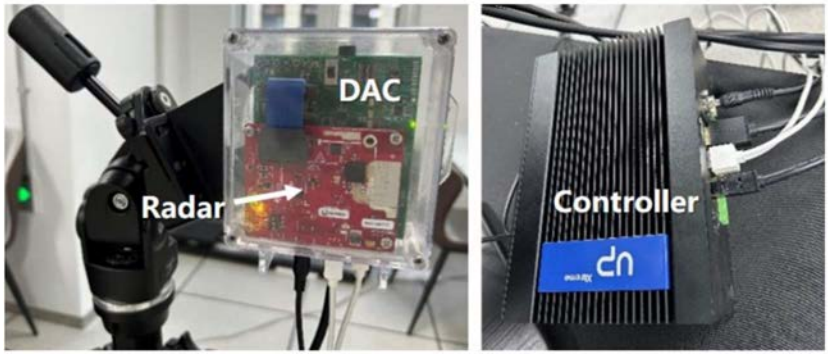

Figure A.1-3: Radar hardware connection

The investigation considered a body height of 1,75 m, where the participant stood directly in front of the radar and only performed arm-swinging movements. In this way, the presence of echoes resulting from body motions can be mitigated, thus, the Doppler features caused by micro-motion can be observed clearly. Just like Figure A.1-4 shows, the person being measured replicates the natural gait pattern of walking, wherein the left arm is positioned behind while the right arm is in the front. This motion is then reciprocated, with the right arm moving to the back and the left arm moving forward, forming a circular movement. A total of 3 swing-arm cycles, equivalent to a duration of 3 s, were recorded.

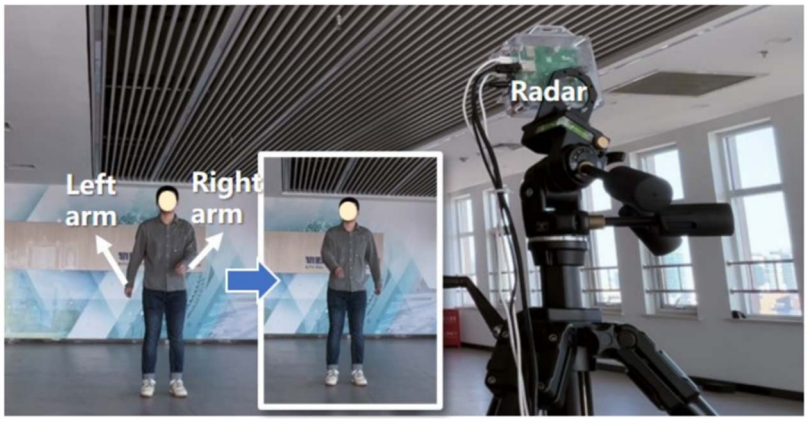

Figure A.1-4: Measurement of swinging arms in front of radar

The results are obtained as shown in Figure A.1-5. The velocity-distance image presented on the left depicts negative velocity for the arm approaching the radar, whereas positive velocity is observed for the arm going away from the radar. While on the right of Figure A.1-5, the Doppler-time image exhibits apparent periodicity in the movements of the left and right arms. Additionally, the swinging arm displays a very regular pattern in continuous time.

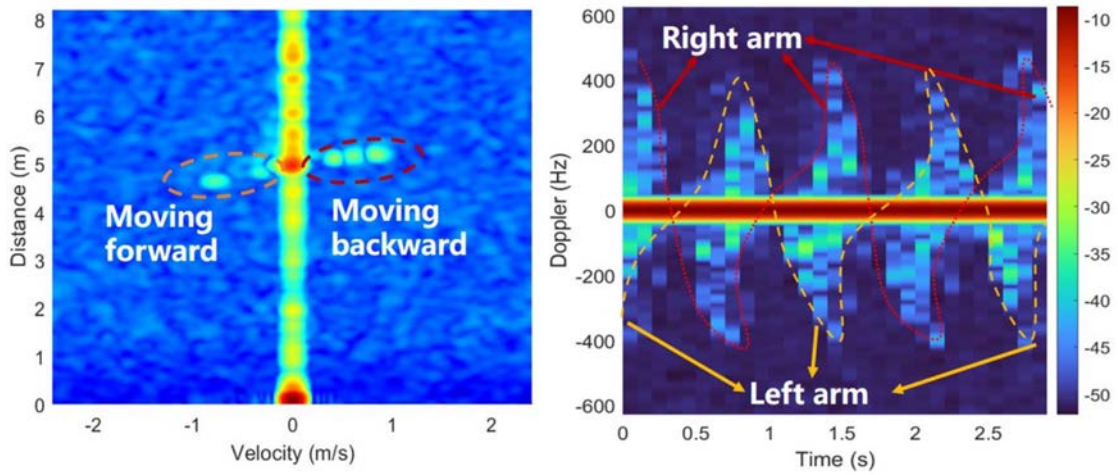

Figure A.1-5: Measurement result: Velocity-Distance plot (left) and Time-Doppler plot (right)

A.2 Ray-tracing simulation

Firstly, it is imperative to ascertain the frequency and propagation mechanism of the simulation according to the measurement system [i.4]. The propagation mechanism for mono-static radar is mainly scattering, and the specific antenna model used is the double-lobe directional scattering model. Secondly, it is essential to model the fixed three-dimensional (3D) scenario and the scatter models, as presented in Figure A.2-1, while also determining the coordinates of the scatter and their moving trajectories. Subsequently, model calibration will be conducted based on the measured data through the adjustment to the Electromagnetic (EM) parameters of the material. Finally, the RT simulation is initiated.

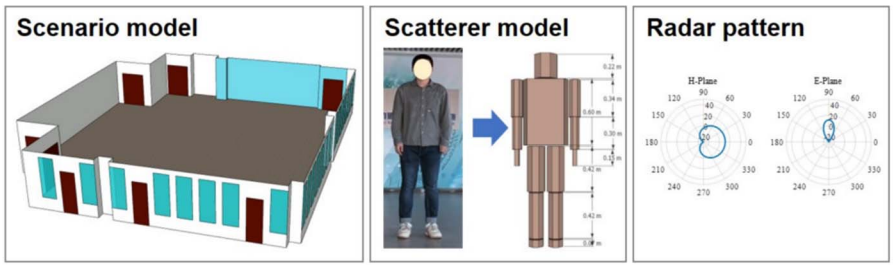

Figure A.2-1: 3D models for the scenario, scatter and antenna pattern

Since the human arm swing is a type of periodic motion, the period of the swing was determined to be 0,5 s in this study based on the measurements, and the residence duration of the arm to its highest point, see Figure A.2-2 before and after the swing was determined to be 0,1 s. While swinging, the two arms are turned inwardly by 30° in the plane of the palms of the hands. The angle of the arm swinging forwardly is set to be positive, while backwardly is negative. Based on observational evidence, it is noticed that the process of human arm swing is not a uniform motion, whose swing angular velocity varies with time. Taking the shoulder as the pivot point of rotation, the speed is the minimum when running to the highest point before and after in the arm's trajectory. This motion is followed by an acceleration towards both sides of the torso. Subsequently, a deceleration occurs as the arm reaches the highest point on the opposite side. This cyclic pattern forms the swinging arm movement.

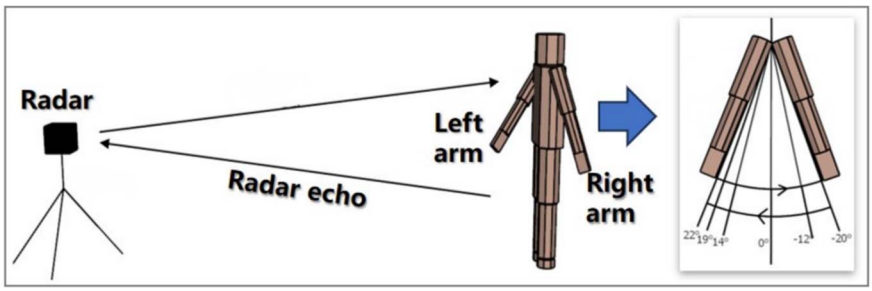

Figure A.2-2: Angle of the arm swing

The ray tracing simulation is triggered, and the results are displayed in Figure A.2-3. It is evident that results regarding Doppler shift, echo signal power, and period are similar to those in figures from A.2-3 to A.2-6. Therefore, RT accurately reproduces the goal scenario.

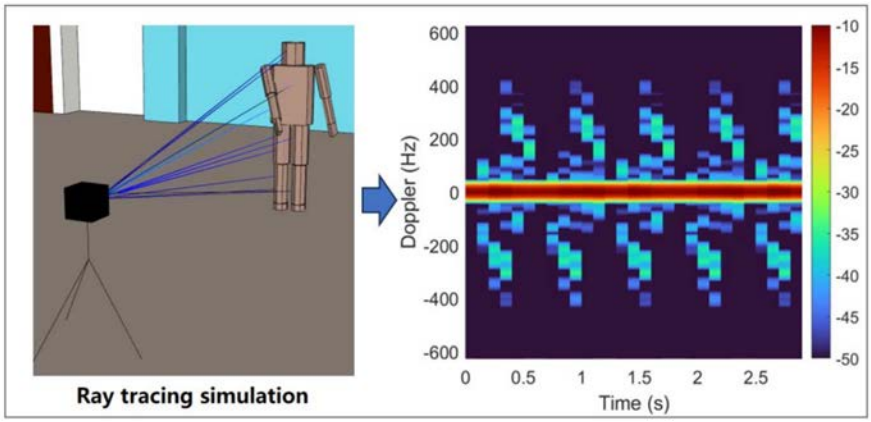

Figure A.2-3: Simulation using RT and the result of Time-Doppler plot

The micro-Doppler features of the multi-angle pedestrian swing arm are investigated due to the angle at which pedestrians appear on the road is random. After calibrating the EM parameters of the materials based on measurements, accurate and efficient RT simulation can be extended for multiple angles/situations. For a more comprehensive study, taking the angle opposite to radar as 0°, four different angles are set to rotate the human body: 0°, 30°, 60° and 90°, seen in Figure A.2-4.

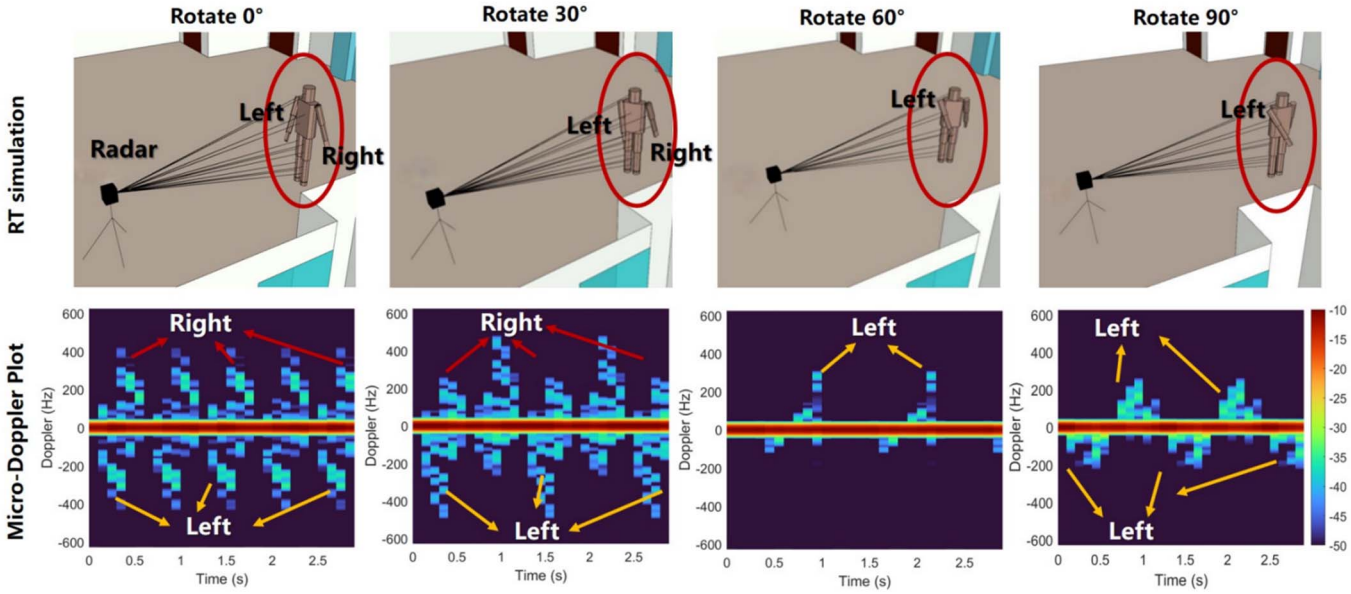

Figure A.2-4: Multiple angles of human rotate their simulation results

It can be clearly observed that the micro-Doppler pattern of the swinging arms changed according to the body angle rotated. Specifically, the regularity changes with radial distance from the radar as well as speed. When the trajectory of the hands is parallel to the line to the radar, the Doppler pattern is distinct, and the amplitude is large. When the hand moves perpendicular to the line-of-sight to the radar, e.g. when rotated to 60°, the Doppler shift detected is quite tiny. The signal appears tooth-like due to the presence of acceleration and deceleration states in the arm waving.

The simulation for human walking is also carried on by ray-tracing simulation. Motion of human walking is modelled firstly by adjust joints of 3D human model, which is given by Figure A.2-5.

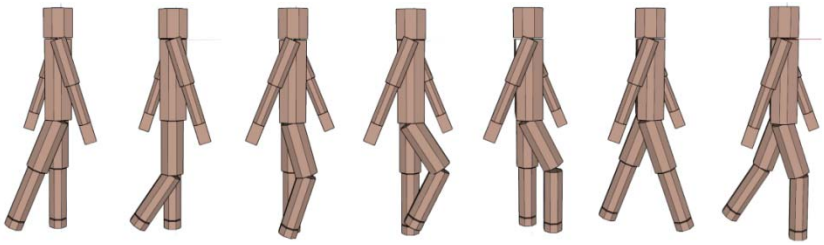

Figure A.2-5: Key-frames of walking human

The micro-Doppler features simulation result of walking human are shown as Figure A.2-6, in which the total micro-Doppler features can be seen as combination of several curves. The red curve is the micro-Doppler feature due to human body. The yellow curves describe micro-Doppler frequency due to left and right arms. The white curves describe micro-Doppler frequency due to left and right legs.

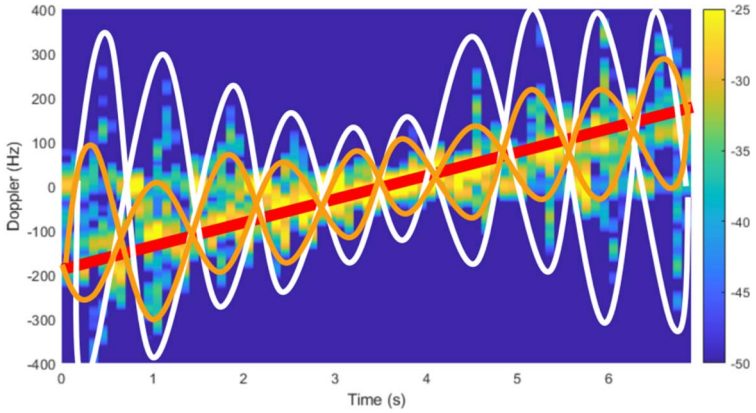

Figure A.2-6: Micro-Doppler features simulation result of walking human

The micro-Doppler curves from legs are studied as a start point. Each curve fits combination of some sine functions.

Table A.2-1: Micro-Doppler function for human

	Micro-Doppler function
Left leg	$f_{micro}(t) = 37{,}59\,sin(\,5{,}97t + 2{,}145)$
Right leg	$f_{micro}(t) = 195{,}2\,sin(\,0{,}5733t + 2{,}766)$

Annex B:
Measurement campaigns for Rain Attenuation

B.1 Measurements for Rain Attenuation Modelling

In this study, a weather darkroom is selected as the measurement scenario because of its ability to provide a highly controlled environment. This setup effectively allows for precise quantification of attenuation characteristics at specific rainfall levels, mitigating the interference from environmental variability. As shown in Figure B.1-1, the measurement system is placed within the rainfall area of the darkroom. The Tx and Rx antennas, securely mounted on brackets, form an integral part of this system. To ensure waterproofing, all cables are covered with orange rubber hoses. Moreover, the Tx and Rx antennas themselves are waterproofed by wrapping their exteriors with waterproof tape and waterproof film. This setup is designed to maintain the integrity of the measurement system under simulated rainfall conditions, in order to obtain reliable data for analysing rain attenuation effects on mmWave signals.

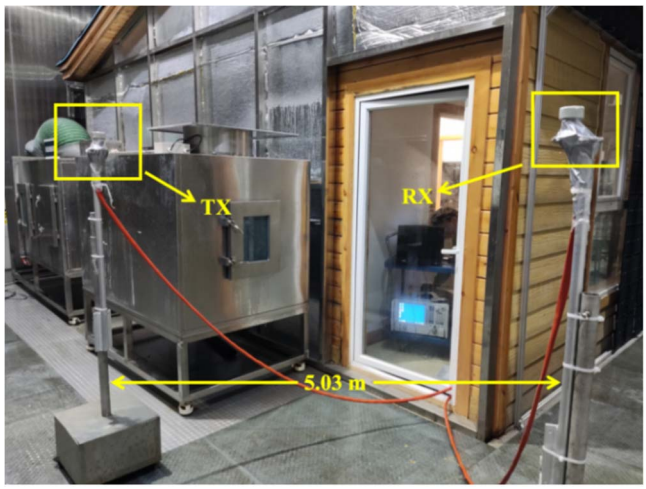

Figure B.1-1: Measurement scenario

The measurement system, depicted in Figure B.1-2 (a), comprises Tx and Rx omnidirectional antennas, two Universal Software Radio Peripherals (USRPs), a Radio Frequency Power Amplifier (RFPA), a frequency converter, and two Personal Computers (PCs) controlled terminal, with 5 m cables used for both Tx and Rx system connections and an additional 1,5 m cable connecting the Tx antenna to the RFPA. To ensure the clock and frequency synchronization of the system, two Global Positioning System (GPS) devices are employed for synchronization between the Tx and the Rx, while the entire measurement system is controlled by two computers. The pattern of the Tx and Rx antennas used in this measurement is presented in Figure B.1-2 (b).

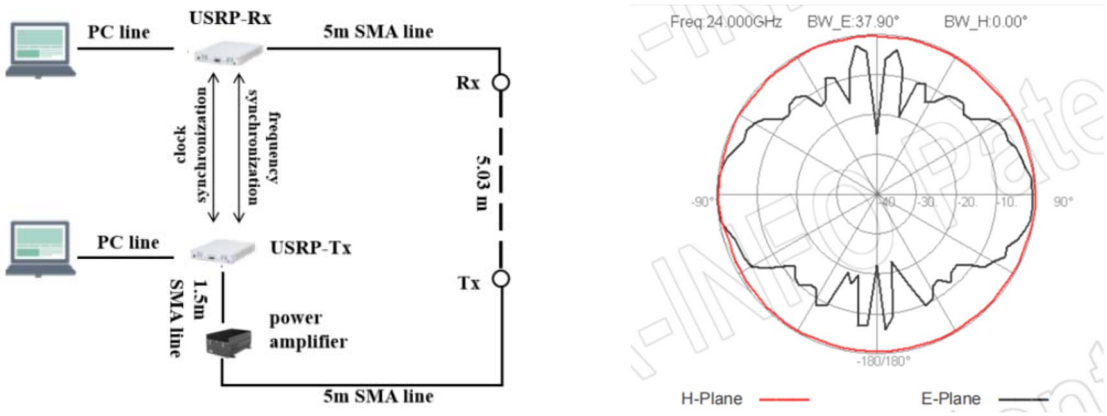

(a) Deployment of measurement system (b) Antenna pattern

Figure B.1-2: Measurement system and antenna pattern

The detailed measurement parameters are presented in Table B.1-1, the measurements are carried out at frequency bands of 24 GHz, 29 GHz, and 38 GHz with a bandwidth of 20 MHz, utilizing a total of 2 048 frequency sampling points. Both the Tx and Rx antennas are set at a height of 1,77 m, employing vertical polarization and offering a 4-dBi gain. The rainfall rates selected for the measurement are 55,4 mm/h, 72,5 mm/h, and 80,2 mm/h, respectively.

Table B.1-1: Measurement configuration

Parameter	Value
Centre frequency [GHz]	24, 29, 38
Bandwidth [MHz]	20
Frequency sampling points	2 048
Antenna height [m]	1,77
Antenna type	Omni-directional
Polarization	Vertical polarization
Antenna gain [dBi]	4
Rainfall rate[mm/h]	55,4, 72,5, 80,2

The measurement data are processed to derive Power Delay Profile (PDP), with 24 GHz and 38 GHz PDP variations under different rainfall rates illustrated in Figure B.1-3 (a) and (b), respectively. Through analysing the PDP, detailed channel information is obtained, reflecting the multipath propagation characteristics within the rain-affected environment. Additionally, the amplitude variations in the PDP can indicate the degree of signal attenuation and distortion caused by rain, with attenuation nonlinear increasing as the rainfall rate and frequency rises. The data obtained and the subsequent analysis provide the foundation for evaluating and optimizing the Recommendation ITU-R P.838-3 [i.42] model.

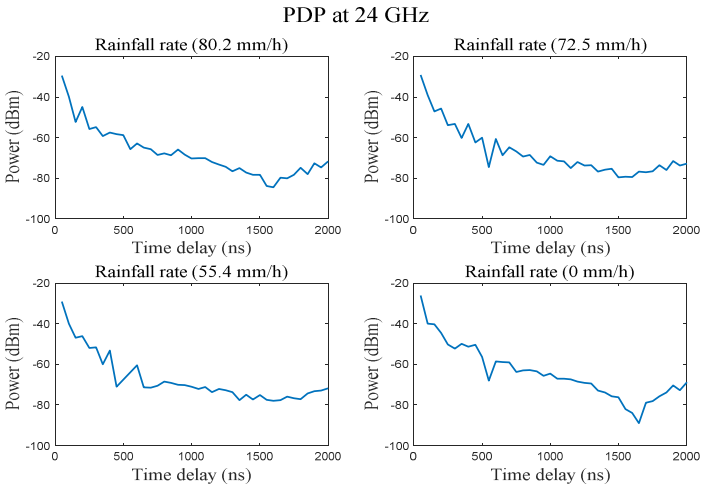

(a) PDP under different rainfall rates at 24 GHz

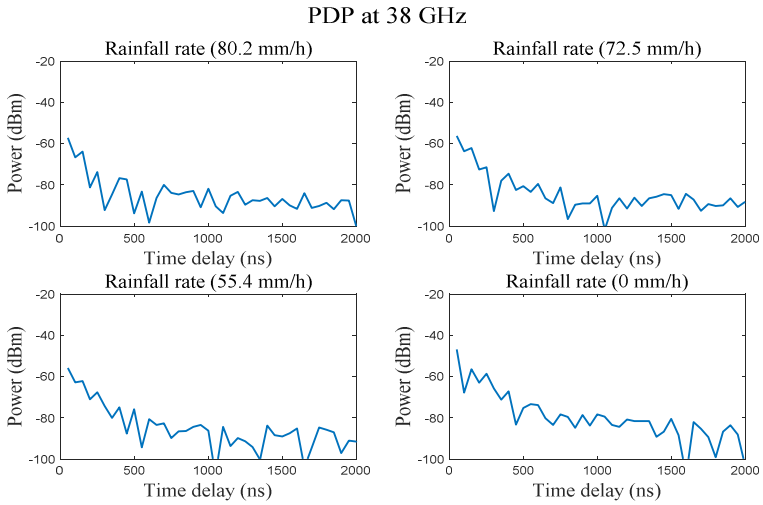

(b) PDP under different rainfall rates at 38 GHz

Figure B.1-3: PDP under different rainfall rates

History

Document history		
V1.1.1	August 2025	Publication